Martin Suda*, Manfried Faber, Joachim Bosina, Tobias Jenke, Christian Käding, Jakob Micko, Mario Pitschmann and Hartmut Abele

Spectra of neutron wave functions in Earth's gravitational field

https://doi.org/10.1515/zna-2022-0050
Received February 17, 2022; accepted April 13, 2022;
published online May 6, 2022

Abstract: The time evolution of a quantum wave packet in the linear gravity potential is known as Quantum Bouncing Ball. The qBounce collaboration recently observed such a system by dropping wave packets of ultracold neutrons by a height of roughly 30 microns. In this article, space and momentum spectra as well as Wigner functions of the neutron wave functions in the gravitational field of the Earth are analyzed. We investigate the quantum states in the "preparation region", into which they transition after exiting a narrow double-mirror system and where we would expect to observe free fall and bounces in classical physics. For this, we start from the stationary solutions and eigenvalues of the Schrödinger equation in terms of Airy functions and their zeros. Subsequently, we examine space and momentum distributions as well as Wigner functions in phase space for pure and mixed quantum states. The possible influence of Yukawa-like forces for small distances of several micrometers from the mirror is included through first order perturbation calculations. Those allow us to study the resulting modifications of space and momentum distributions, and phase space functions.

Keywords: gravitation; neutron; qBounce; Wigner function; Yukawa forces.

PACS number: 03.65.Ge.

***Corrresponding author**: **Martin Suda**, AIT, Austrian Institute of Technology, Giefinggasse 4, 1210 Vienna, Austria; and Technische Universität Wien, Atominstitut, Stadionallee 2, 1020 Vienna, Austria, E-mail: martin.suda@ait.ac.at

Manfried Faber, **Christian Käding**, **Mario Pitschmann and Hartmut Abele**, Technische Universität Wien, Atominstitut, Stadionallee 2, 1020 Vienna, Austria, E-mail: manfried.faber@tuwien.ac.at (M. Faber), hartmut.abele@tuwien.ac.at (H. Abele)

Joachim Bosina and Jakob Micko, Technische Universität Wien, Atominstitut, Stadionallee 2, 1020 Vienna, Austria; and Institut Laue-Langevin - 71 avenue des Martyrs CS 20156, 38042, Grenoble Cedex 9, France

Tobias Jenke, Institut Laue-Langevin - 71 avenue des Martyrs CS 20156, 38042, Grenoble Cedex 9, France

1 Introduction

A quantum wave packet bouncing on a hard surface under the influence of gravity has drawn some attention in the literature due to its departures from classical behaviour [1–7]. Other aspects of this quantum bouncer have also been studied to some extent. Of those, we would like to mention its chaotic behavior [8], the mathematical basis with orthonormal Airy eigenfunction solutions [9], the Wigner phase space as an interface of gravity and quantum mechanics [10], quantum revivals in a periodically driven gravitational cavity [11], and inertial and gravitational mass in quantum mechanics [12]. The development of sufficient ultracold neutron sources at the Institut Laue Langevin (ILL) in Grenoble and techniques to manipulate neutrons with high precision have made the simple quantum bouncer experimentally realizable. Demonstrations of quantum states in the gravitational potential of the Earth can be found in [13–15] and aspects from a more theoretical point of view in [16, 17]. From the beginning these experiments were used to constrain hypothetical gravity-like interactions [18–20].

In this article, we will examine some details of the bounce of a neutron wave packet closely related to an experimental realization by the *q*Bounce collaboration. More precisely, we will investigate the behavior of the momentum space wave packet solutions, the widths of the position and momentum space wave packets during the "bounce", and aspects of Yukawa-type interactions. Extensive use of the Wigner function formalism as a function of time is made as well.

The *q*Bounce experiment has been performed at the UCN-beam position of the PF2 instrument at ILL, so far the 7th strongest source for ultracold neutrons with high continuous fluence, which is ideal for quantum bouncer realizations. It tests gravity at small distances with quantum interference techniques. The experimental tool is a gravitationally interacting quantum system – an ultracold neutron in the gravitational potential of the Earth – and a reflecting mirror above which the neutron is bound in well-defined quantum states. The collaboration is continuously developing a gravity resonance spectroscopy (GRS) [21–25] technique, which allows for a clear identification

Open Access. © 2022 the author(s), published by De Gruyter. This work is licensed under the Creative Commons Attribution 4.0 International License.

of the measured energy eigenstates states $|1\rangle \to |2\rangle$, $|1\rangle \to |3\rangle$, $|1\rangle \to |4\rangle$, $|2\rangle \to |3\rangle$, $|2\rangle \to |4\rangle$, $|2\rangle \to |5\rangle$, and most recently $|1\rangle \to |6\rangle$. In this way, precisions are reached which enable us to search for hypothetical gravity-like interactions with relevance for cosmology. So far limits for axions [22], chameleon [23] and symmetron fields [24] have been placed.

For the purpose of this article, an important observable is the spatial density distribution of a free falling neutron above a reflecting mirror. A newly developed position-dependent neutron detector makes it possible to visualize the square of the Schrödinger wave function [26, 27]. Detailed descriptions of these processes can be found in [28]. We now have a high-precision gravitational neutron spectrometer with available spatial resolution of 1.5 μm at our disposal. Neutrons are detected in CR-39 track detectors after neutron capture in a coated Boron-10 layer of 100 nm thickness. An etching technique makes the tracks visible with a length of about 3 µm–6 µm [29].

Because of the Schrödinger equation, and therefore by means of the quantum mechanical description of particles in a gravitational field, a wave function is established exhibiting both, a local spreading and a momentum distribution. As is well-known, it is possible to describe this phenomenon using Airy functions. In doing so, it appears that, due to the reflection on the mirror surface, a ground state and excited states emerge. Moreover, the Wigner function allows for a combined view within the entire phase space. Further attention is especially put on marginal distribution functions of the Wigner distribution which correspond exactly to the space and momentum distributions. For all our numerical calculations we use the computer software *Mathematica*. The space distribution had been measured using a track detector [29]. Likewise, the momentum distribution should be determined experimentally using an appropriate detector. The main objective of our calculations is the comparison with these measurements.

The article is organized as follows: In chapter 2 the Schrödinger equation including a gravitational potential is given and time-independent solutions are explored. Using an appropriate scaling, a differential equation is found, whose solutions can be expressed by Airy functions. The calculation of the Fourier transform of the ground state is presented and excited states are considered. Furthermore, the solutions using the Wigner function and the time dependence of the superposition of ground and first excited states are described. In chapter 3 we investigate the *q*Bounce-system in which the neutron wave is enclosed between 2 mirrors. This chapter is subdivided into two sections, one dealing with the Fourier transformation of the wave function and the other one being concerned with the Wigner function. Chapter 4 is dedicated to a wave function exiting the double mirror system and falling onto a subsequent mirror. One section describes the space distribution in this "free fall" region, another one is dedicated to the space distribution of mixtures, the third one deals with the calculation of the momentum distribution and the last section presents the related Wigner function. In chapter 5 we perform a first order perturbation calculation in order to describe a very small change in the potential near the mirror. At first, the mathematical background is presented. Afterwards, the Fourier transformations of the results are carried out, the momentum distribution including a Yukawa-like term described and the related space distribution evaluated. A discussion and proposed applications of the Yukawa correction including possible experimental results are added. Finally, chapter 6 gives a short summary.

2 Schrödinger equation for *q*Bounce

In this section we specify the Schrödinger equation of neutrons in the gravitational field. Because of an infinitely hard mirror where the neutrons impinge (qBounce) well known stationary solutions of the wave function (eigenfunctions) are found in terms of Airy-functions. The energy eigenvalues are linked to the zeros of these functions. Furthermore the Fourier transform of the ground state and of excited states are calculated and graphically displayed. The Wigner function of these states is presented. The time-dependence of coherent and incoherent mixtures of ground and excited states are investigated. The basic idea behind this section is to prepare for the following Section 3 where the neutron beam is enclosed between 2 mirrors.

The time-dependent Schrödinger equation for a neutron with mass m_{N} in the gravitational field of the Earth with potential energy (g is the gravitational acceleration, z the distance above the mirror)

$$V(z) = m_{\mathrm{N}} g z \tag{1}$$

reads

$$\hat{H}\,\psi(z,t) = \mathrm{i}\hbar\,\dot{\psi}(z,t), \tag{2}$$

where $\hat{H}$ is the Hamiltonian containing $V(z)$. The energy of the wave function $\psi(z,t)$ is quantized in the potential $V(z)$. Using the ansatz

$$\psi_n(z,t) = \mathrm{e}^{-\mathrm{i}\frac{E_n}{\hbar}t}\psi_n(z) \tag{3}$$

for a stationary state of energy E_n with $n = 1, 2, \ldots$, we obtain the time-independent Schrödinger equation

$$\left[-\frac{\hbar^2}{2m_\mathrm{N}}\frac{\mathrm{d}^2}{\mathrm{d}z^2} + m_\mathrm{N} g z\right]\psi_n(z) = E_n \psi_n(z). \tag{4}$$

For negative values of z we have $\psi(z) = 0$ because the particles cannot enter the mirror surface. Therefore, the boundary condition for the solution of the differential equation is $\psi(0) = 0$. For this reason, it is supposed that the surface of the mirror has an infinite Fermi potential and the quantum wave does not enter the surface. This is of course just an approximation.

At this point, it is appropriate to mention that the problem of two mirrors as well as the transition from an inertial frame (z_0, t_0) to a non-inertial frame (z, t) has already been described in [30].

Searching for solutions $\psi_n(z)$, we multiply Eq. (4) with the factor $\left(\frac{2}{\hbar^2 m_\mathrm{N} g^2}\right)^{1/3}$ and, using the substitutions [28]

$$\begin{aligned} \zeta &= z/z_0, \quad z_0 = \left(\frac{\hbar^2}{2m_\mathrm{N}^2 g}\right)^{1/3} \approx 5.86796\,\mu\mathrm{m}, \\ a_n &= -E_n/E_0, \quad E_0 = \left(\frac{\hbar^2 m_\mathrm{N} g^2}{2}\right)^{1/3} \approx 0.602\,\mathrm{peV}, \end{aligned} \tag{5}$$

where E_0 is a characteristic gravitational energy scale, we obtain the differential equation

$$\left(\frac{\mathrm{d}^2}{\mathrm{d}\zeta^2} - (\zeta + a_n)\right)\psi_n(\zeta) = 0. \tag{6}$$

Comparing this equation with the Airy equation

$$\left(\frac{\mathrm{d}^2}{\mathrm{d}\zeta^2} - \zeta\right)\mathrm{Ai}(\zeta) = 0, \tag{7}$$

we notice that the (non-normalized) eigenfunctions $\psi_n(\zeta)$ can be expressed through the Airy function $\mathrm{Ai}(\zeta)$ by moving the origin of coordinates to the nth zero point a_n:

$$\psi_n(\zeta) = \mathrm{Ai}(\zeta + a_n)\Theta(\zeta). \tag{8}$$

As described in [30] the normalized wave function $\psi_n(z, t)$ is given by

$$\begin{aligned} \psi_n(z,t) &= \frac{1}{\sqrt{z_0}\mathrm{Ai}'\left(-\frac{z_n}{z_0}\right)}\mathrm{Ai}\left(\frac{z - z_n}{z_0}\right)\mathrm{e}^{-\frac{\mathrm{i}}{\hbar}E_n t} \\ &= \psi_n(z)\,\mathrm{e}^{-\frac{\mathrm{i}}{\hbar}E_n t}. \end{aligned} \tag{9}$$

The first zero point of the Airy function is located at $a_1 \approx -2.3381$. This means, that $E_1 = -a_1 E_0 \approx 1.41$ peV. Additional zero points are located along the negative axis, as can be seen in Figure 1. They determine the energy eigenvalues E_n according to Eq. (5). We list some of them below ($z_n = -z_0 a_n$):

$$\begin{aligned} &n = 1, \quad E_1 \approx 1.40672\,\mathrm{peV}, \quad z_1 \approx 13.71680\,\mu\mathrm{m}, \\ &\quad a_1 \approx -2.33810, \\ &n = 2, \quad E_2 \approx 2.45951\,\mathrm{peV}, \quad z_2 \approx 23.98246\,\mu\mathrm{m}, \\ &\quad a_2 \approx -4.08795, \\ &n = 3, \quad E_3 \approx 3.32144\,\mathrm{peV}, \quad z_3 \approx 32.38707\,\mu\mathrm{m}, \\ &\quad a_3 \approx -5.52056, \\ &n = 4, \quad E_4 \approx 4.08321\,\mathrm{peV}, \quad z_4 \approx 39.81502\,\mu\mathrm{m}, \\ &\quad a_4 \approx -6.78671, \\ &n = 5, \quad E_5 \approx 4.77958\,\mathrm{peV}, \quad z_5 \approx 46.60526\,\mu\mathrm{m}, \\ &\quad a_5 \approx -7.94412, \\ &n = 6, \quad E_6 \approx 5.42846\,\mathrm{peV}, \quad z_6 \approx 52.93243\,\mu\mathrm{m}, \\ &\quad a_6 \approx -9.02262. \end{aligned} \tag{10}$$

The quantities z_n are given, such that they can later be compared to Eq. (29).

Concerning the calculation of the spectra and the Wigner function, the following formalism is developed using the example of the ground state. The wave function of the ground state $\psi_1(\zeta)$ can be written as $\psi_1(\zeta) = \mathrm{Ai}(\zeta + a_1)\Theta(\zeta)$, where $\Theta(\zeta)$ is Heaviside's step function, see Figure 2(a). This Heaviside step function is necessary in order to fulfill the boundary condition caused by the mirror whereupon the wave function has to be zero for negative ζ–values.

The spatial distribution is given by $|\psi_1(\zeta)|^2$. This function can be taken from Figure 1, orange curve, by imagining that the curve is shifted by a_1 to the positive ζ–axis.

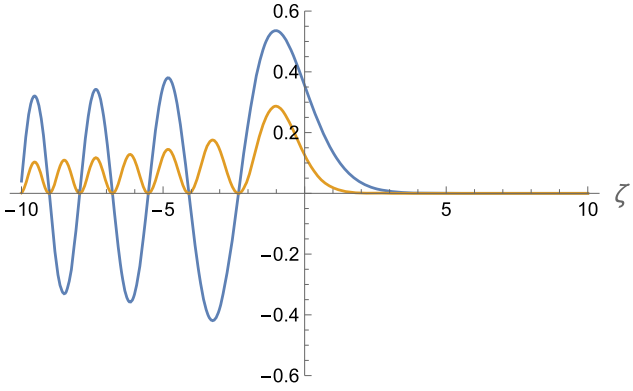

Figure 1: Airy function $\mathrm{Ai}(\zeta)$ (blue) and $[\mathrm{Ai}(\zeta)]^2$ (orange).

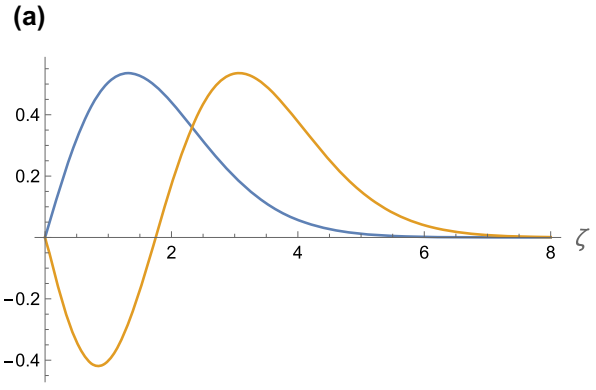

Figure 2: Wave functions and momentum distributions of the ground state with $a_1 \approx -2.3381$ and the first excited state with $a_2 \approx -4.08795$.

2.1 Calculation of Fourier transform of ground state

In order to attain the momentum space (variable k), the wave function $\psi_1(\zeta)$ has to be Fourier transformed:

$$\begin{aligned} F(k, a_1) &= \frac{1}{\sqrt{2\pi}} \int_{-\infty}^{\infty} \mathrm{e}^{-\mathrm{i}\zeta k} \mathrm{Ai}(\zeta + a_1)\Theta(\zeta)\,\mathrm{d}\zeta \\ &= \frac{1}{\sqrt{2\pi}} \int_{0}^{\infty} [\cos(\zeta k) - \mathrm{i}\sin(\zeta k)]\mathrm{Ai}(\zeta + a_1)\,\mathrm{d}\zeta \\ &=: f_\mathrm{c}(k, a_1) - \mathrm{i} f_\mathrm{s}(k, a_1), \end{aligned} \tag{11}$$

where the two functions

$$\begin{aligned} f_\mathrm{c}(k, a_1) &:= \frac{1}{\sqrt{2\pi}} \int_{0}^{\infty} \cos(\zeta k)\mathrm{Ai}(\zeta + a_1)\,\mathrm{d}\zeta, \\ f_\mathrm{s}(k, a_1) &:= \frac{1}{\sqrt{2\pi}} \int_{0}^{\infty} \sin(\zeta k)\mathrm{Ai}(\zeta + a_1)\,\mathrm{d}\zeta \end{aligned} \tag{12}$$

have been defined. They are displayed in Figure 3. It should be mentioned that Fourier integrals of Airy-functions of this type (or similar expressions throughout the paper) have to be calculated numerically using *Mathematica*. To the best of our knowledge we did not find any analytical results of such integrals.

The momentum spectrum is given by

$$|F(k, a_1)|^2 = [f_\mathrm{c}(k, a_1)]^2 + [f_\mathrm{s}(k, a_1)]^2, \tag{13}$$

see Figure 2(b). We have to stress that k is actually a dimensionless variable and related to the physical momentum k_p by

$$k = \frac{z_0}{\hbar} k_\mathrm{p}. \tag{14}$$

2.2 Excited states

Here we look at the excited states by discussing their momentum spectra for a few selected example values of n. The first excited state is characterized by the second zero point $a_2 \approx -4.08795$ of the Airy function. Its wave function and momentum spectrum are depicted in Figure 2(a) and (b), respectively.

The third zero point of the Airy function is located at $a_3 \approx -5.52056$ (2nd excited state) and yields a momentum spectrum as given in Figure 4. Besides, this figure also shows the results for the 3rd and 9th excited states with the corresponding fourth and tenth zero points $a_4 \approx -6.78671$ and $a_{10} \approx -12.8288$ of the Airy function.

In Figure 4 we can see that the number of oscillations before the onset of the asymptotic behavior of the momentum spectra increases with n. In case of n towards infinity,

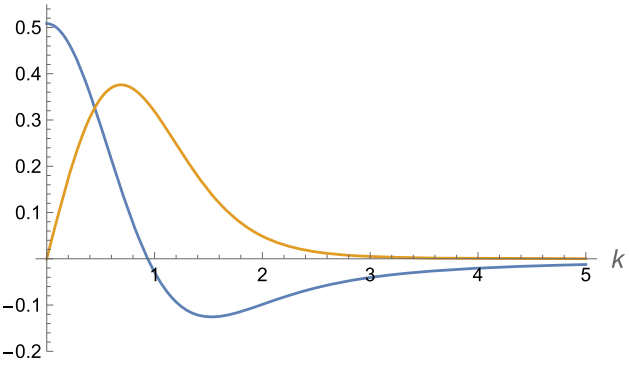

Figure 3: $f_\mathrm{c}(k, a_1)$ with $a_1 \approx -2.3381$ (blue) and $f_\mathrm{s}(k, a_1)$ with $a_1 \approx -2.3381$ (orange).

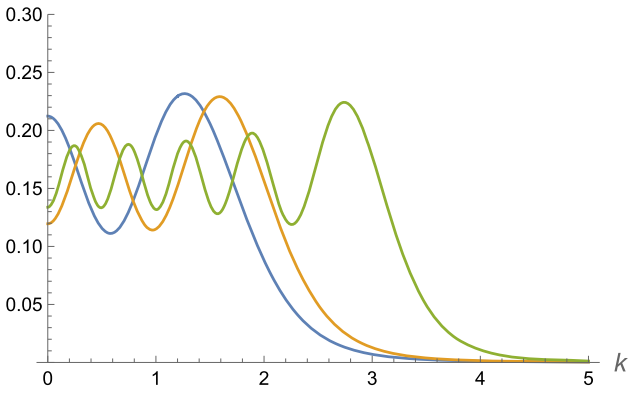

Figure 4: Momentum distributions of the second excited state $|F(k,a_3)|^2$ with $a_3 \approx -5.52056$ (blue), the third excited state $|F(k,a_4)|^2$ with $a_4 \approx -6.78671$ (orange), and the ninth excited state $|F(k,a_{10})|^2$ with $a_{10} \approx -12.8288$ (green).

the amplitudes of the oscillations tend to zero and the momentum spectrum becomes a constant.

2.3 Presentation using Wigner function

The 2-dimensional Wigner function is an important tool in quantum optics. It allows for a simultaneous view into space and momentum regions. The Wigner function is real but can be positive and negative as well. In this respect, it is not a classical 2-dim distribution function. Therefore, it is often called a quasi-distribution function. Most remarkably is the property that an integration of a Wigner function over momentum gives the spatial probability, while integration over the spatial coordinate gives the momentum probability. These two marginal distribution functions (spatial and momentum distributions) are, at least in principle, experimentally accessible. The Wigner function formalism has already been applied within the framework of investigations of the gravitational potential of the Earth [12]. In addition, we would like to point to an article, in which the interface of gravity and quantum mechanics has been discussed with the Wigner phase space distribution function [10].

For our purposes, we will use the Wigner function in order to recover the momentum spectrum Eq. (13). The definition of the Wigner function is [31]:

$$W(\zeta,k) := \frac{1}{2\pi}\int_{-\infty}^{\infty} \mathrm{e}^{\mathrm{i}\zeta' k}\,\psi^*\left(\zeta+\frac{\zeta'}{2}\right)\psi\left(\zeta-\frac{\zeta'}{2}\right)\mathrm{d}\zeta'. \tag{15}$$

Plugging Eq. (8) into this definition, we find

$$W(\zeta,k,a_n) = \frac{1}{2\pi}\int_{-\infty}^{\infty} \mathrm{e}^{\mathrm{i}\zeta' k}\,\mathrm{Ai}\left(\zeta+\frac{\zeta'}{2}+a_n\right)\Theta\left(\zeta+\frac{\zeta'}{2}\right) \times \mathrm{Ai}\left(\zeta-\frac{\zeta'}{2}+a_n\right)\Theta\left(\zeta-\frac{\zeta'}{2}\right)\mathrm{d}\zeta', \tag{16}$$

which is obviously symmetric in k: $W(\zeta,k,a_n) = W(\zeta,-k,a_n)$.

Due to $\frac{1}{2\pi}\int_{-\infty}^{\infty}\mathrm{e}^{\mathrm{i}\zeta' k}\,\mathrm{d}k = \delta(\zeta')$, we can easily see how integration over the momentum k yields the space distribution:

$$\int_{-\infty}^{\infty} W(\zeta,k,a_n)\,\mathrm{d}k = [\mathrm{Ai}(\zeta+a_n)\,\Theta(\zeta)]^2 = |\psi_n(\zeta)|^2. \tag{17}$$

The Wigner function in Eq. (16) can be rewritten as:

$$W(\zeta,k,a_n) = \frac{1}{\pi}\int_{0}^{\infty} \cos(\zeta' k)\mathrm{Ai}\left(\zeta+\frac{\zeta'}{2}+a_n\right)\Theta\left(\zeta+\frac{\zeta'}{2}\right) \times \mathrm{Ai}\left(\zeta-\frac{\zeta'}{2}+a_n\right)\Theta\left(\zeta-\frac{\zeta'}{2}\right)\mathrm{d}\zeta'. \tag{18}$$

Using Eq. (18), we can find the momentum distribution by integrating over ζ:

$$\begin{aligned} |F(k,a_n)|^2 &= \int_{-\infty}^{\infty} W(\zeta,k,a_n)\,\mathrm{d}\zeta \\ &= \frac{1}{\pi}\int_{0}^{\infty}\cos(\zeta' k)\,f(\zeta',a_n)\,\mathrm{d}\zeta', \\ f(\zeta',a_n) &:= \int_{\frac{\zeta'}{2}}^{\infty}\mathrm{Ai}\left(\zeta+\frac{\zeta'}{2}+a_n\right)\mathrm{Ai}\left(\zeta-\frac{\zeta'}{2}+a_n\right)\mathrm{d}\zeta, \\ &\zeta' \geq 0. \end{aligned} \tag{19}$$

Evaluating this expression numerically for the states considered in Figure 2(b), we obtain the same results as in these figures. Consequently, the Wigner function provides us with a second option to calculate $|F(k,a_n)|^2$.

The 2-dim Wigner function Eq. (18) of the ground state $W(\zeta,k,a_1)$ is plotted in Figure 5(a). It is almost everywhere positive. There are only very small and hardly visible negative regions.

The negative regions are much more visible for the Wigner functions of the first and second excited states, which are plotted in Figure 5(b) and (c), respectively. This negativity distinguishes the Wigner distribution from the always strictly positive spatial and momentum distributions. In Figure 5(d) the ninth excited state is plotted. As a

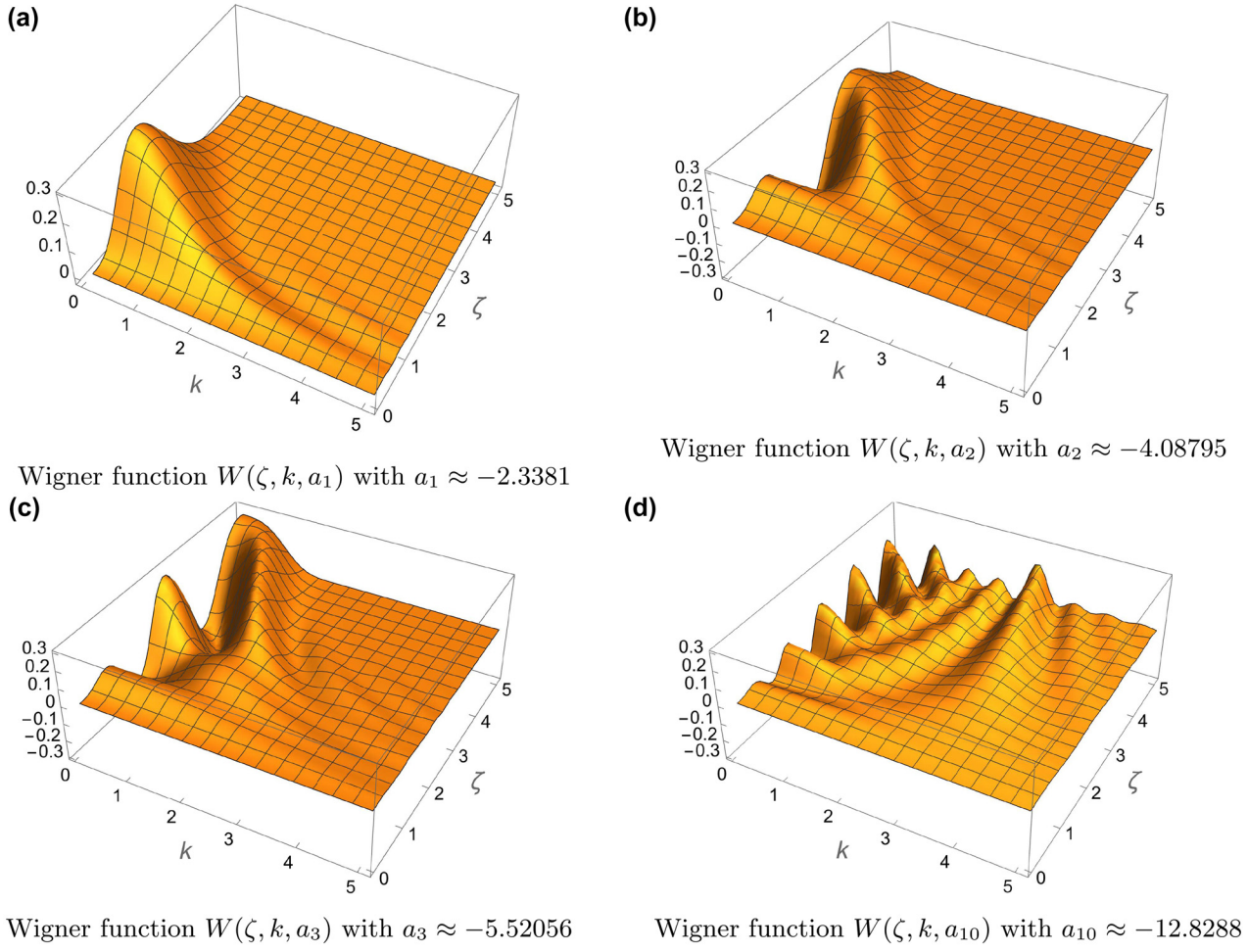

Wigner function $W(\zeta, k, a_1)$ with $a_1 \approx -2.3381$

Wigner function $W(\zeta, k, a_2)$ with $a_2 \approx -4.08795$

Wigner function $W(\zeta, k, a_3)$ with $a_3 \approx -5.52056$

Wigner function $W(\zeta, k, a_{10})$ with $a_{10} \approx -12.8288$

Figure 5: Wigner functions of the ground state and first, second and ninth excited state.

consequence, a great deal of oscillations can be observed together with a slight decrease of their amplitudes for increasing quantum number. This can be understood because of interference in phase space. A similar behaviour we observe for the momentum distribution in Figure 4 in case of a_{10} where the Wigner function has been integrated over ζ.

2.4 Time-dependence of a mixture of ground state and first excited state

The spatial probability density has been experimentally verified for ultracold neutrons in [23]. Here we suggest that the momentum probability distributions could be measured in a similar fashion. For example, if the ground state population amounts to 70% ($p_1 = 0.7$), the first excited state amounts to 30% ($p_2 = 0.3$), and no other excited states are populated, then extracting the total probability distributions from Figure 2(b) is straightforward. This is because the relative contributions can be extracted from the figures: $\sum_n p_n |F(k, a_n)|^2$, see Figure 6. The orange line in Figure 6 presents an example for $p_1 = p_2 = 0.5$. In this case, the first excited state, represented by $|F(k, a_2)|^2$ and Figure 2(b), is clearly visible. It should be mentioned that this procedure corresponds to an incoherent superposition.

Therefore, the proposed procedure is not exact. We have to take the time dependence of the wave function, see Eq. (3), into account. Consequently, we will now go back to the time-dependent space distribution $|\psi(\zeta, t)|^2$ using the following ansatz of coherent superposition

$$\psi_s(\zeta, t) = \sqrt{p_1} e^{-i\frac{E_1}{\hbar}t} \psi_1(\zeta) + \sqrt{p_2} e^{-i\frac{E_2}{\hbar}t} \psi_2(\zeta), \qquad (20)$$

where $\psi_1(\zeta) = \mathrm{Ai}(\zeta + a_1)\Theta(\zeta)$ and $\psi_2(\zeta) = \mathrm{Ai}(\zeta + a_2)\Theta(\zeta)$ are real functions, and we ignore a potential phase between both terms for simplicity. The time-dependent position probability of this superposition state is therefore

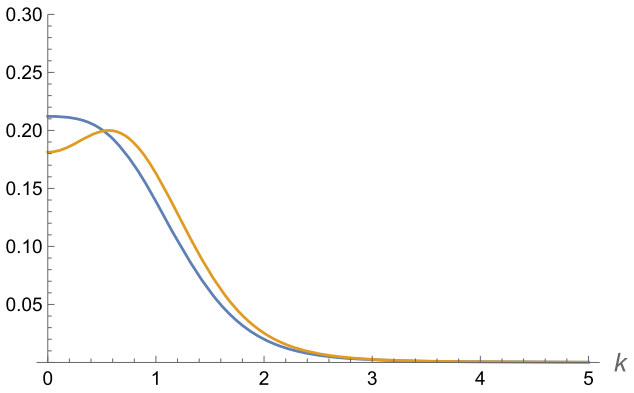

Figure 6: Combined momentum distributions of the ground state and the first excited state $p_1|F(k,a_1)|^2 + p_2|F(k,a_2)|^2$ with $p_1 = 0.7$ and $p_2 = 0.3$ (blue), and $p_1 = p_2 = 0.5$ (orange).

$$|\psi_s(\zeta,t)|^2 = p_1[\mathrm{Ai}(\zeta+a_1)\,\Theta(\zeta)]^2 + p_2[\mathrm{Ai}(\zeta+a_2)\,\Theta(\zeta)]^2 + 2\sqrt{p_1p_2}\,\mathrm{Ai}(\zeta+a_1)\,\mathrm{Ai}(\zeta+a_2)\,\Theta^2(\zeta) \times \cos\left(\frac{E_1-E_2}{\hbar}t\right). \quad (21)$$

This function oscillates with time t. If $p_1 = 1$ and $p_2 = 0$, we recover $|\psi_1(\zeta)|^2$, which is the square of the function depicted in blue in Figure 2(a). Furthermore, we have

$$\frac{E_1-E_2}{\hbar} = \frac{E_0}{\hbar}(-a_1+a_2) \approx 1600.4\,\mathrm{Hz}. \quad (22)$$

This means, that $|\psi_s(\zeta,t)|^2$ oscillates in the time-range of milliseconds, as can be seen in the example shown in Figure 7(a). The first small peak at $t = 0$ appears at $\zeta \approx 2.5$ and not at $\zeta \approx 1.3$, i.e., the maximum of $\psi_1(\zeta)$, see Figure 2(a), because the interference term in Eq. (21) contains $\mathrm{Ai}(\zeta + a_2)$, which is negative in the region between $\zeta = 0$ and $\zeta \approx 1.7$, see Figure 2(a). However, the large maximum at $t \approx 0.002$ s appears for $\zeta \approx 1.3$ due to $\psi_1(\zeta)$ and $p_1 = 0.7$. We assume that such properties of time-dependent position probabilities for superpositions of ground and excited states can be measured.

We have to point out that in case of a non-time-resolving measurement we have to integrate time t in Eq. (21) over one time period, e.g., from 0 to $2\pi\hbar/(E_1 - E_2)$. In this case, the interference term disappears and we obtain only the first two terms $|\psi|^2 = p_1[\mathrm{Ai}(\zeta+a_1)\,\Theta(\zeta)]^2 + p_2[\mathrm{Ai}(\zeta+a_2)\,\Theta(\zeta)]^2$. Figure 8 depicts an example. This spatial probability density is very similar to the results of an experiment using a track detector [23].

The Fourier transform of $\psi_s(\zeta)$ in Eq. (20) reads

$$F_s(k,t) = \sqrt{p_1}\,\mathrm{e}^{-\mathrm{i}\frac{E_1}{\hbar}t}F(k,a_1) + \sqrt{p_2}\,\mathrm{e}^{-\mathrm{i}\frac{E_2}{\hbar}t}F(k,a_2). \quad (23)$$

Next, we want to calculate $|F_s(k,t)|^2$. We obtain

$$|F_s(k,t)|^2 = p_1|F(k,a_1)|^2 + p_2|F(k,a_2)|^2 + \sqrt{p_1p_2}(\alpha\beta^* + \alpha^*\beta), \quad (24)$$
$$\alpha = \mathrm{e}^{\mathrm{i}\frac{(E_1-E_2)}{\hbar}t}, \quad \beta^* = F^*(k,a_1)F(k,a_2).$$

Using Eq. (11) in order to decompose β^*, we find

$$\beta^* = f_c(k,a_1)f_c(k,a_2) + f_s(k,a_1)f_s(k,a_2) + \mathrm{i}\,[f_s(k,a_1)f_c(k,a_2) - f_c(k,a_1)f_s(k,a_2)]. \quad (25)$$

Since $\alpha\beta^* + \alpha^*\beta = 2[\mathrm{Re}(\alpha)\mathrm{Re}(\beta) + \mathrm{Im}(\alpha)\mathrm{Im}(\beta)]$, the final expression for $|F_s(k,t)|^2$ is

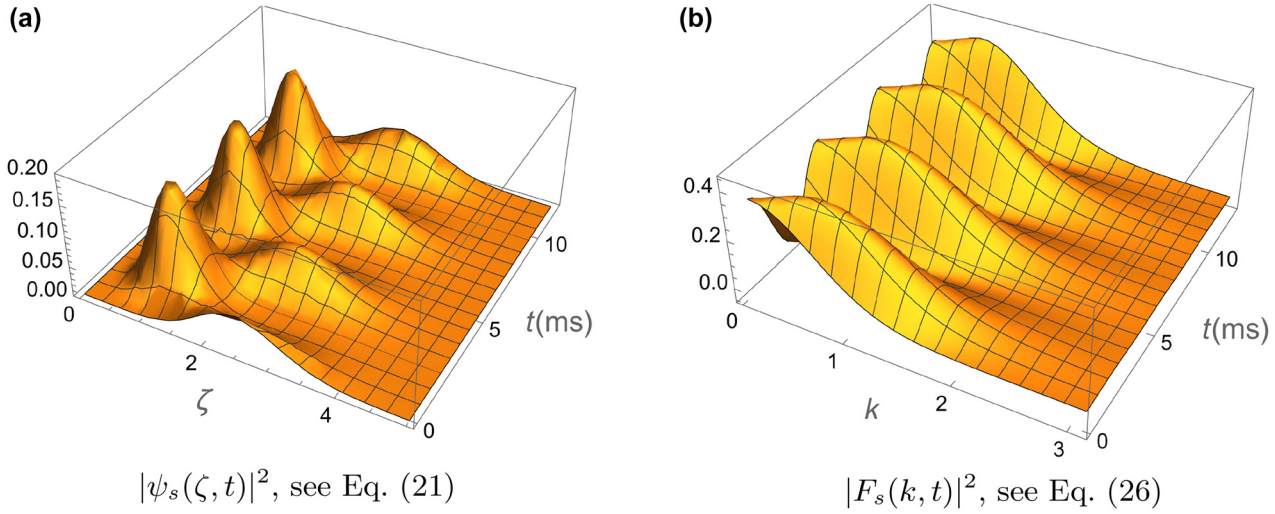

Figure 7: Time-dependent position and momentum probabilities of superposition of the ground state and first excited state with $p_1 = 0.7$ and $p_2 = 0.3$.

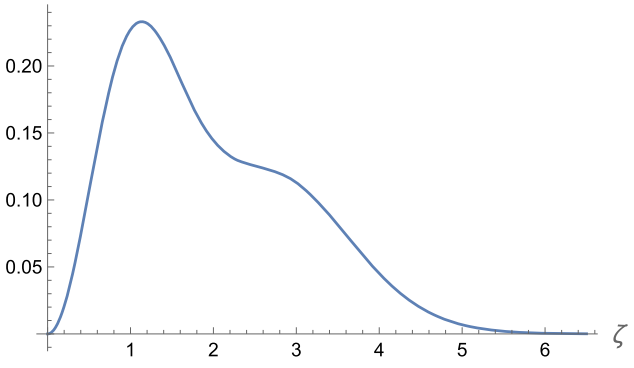

Figure 8: Non-time-resolving position probability $|\psi|^2 = p_1[\mathrm{Ai}(\zeta + a_1)\,\Theta(\zeta)]^2 + p_2[\mathrm{Ai}(\zeta + a_2)\,\Theta(\zeta)]^2$ of superposition of ground state and first excited state, see Eq. (21), with $p_1 = 0.7$ and $p_2 = 0.3$.

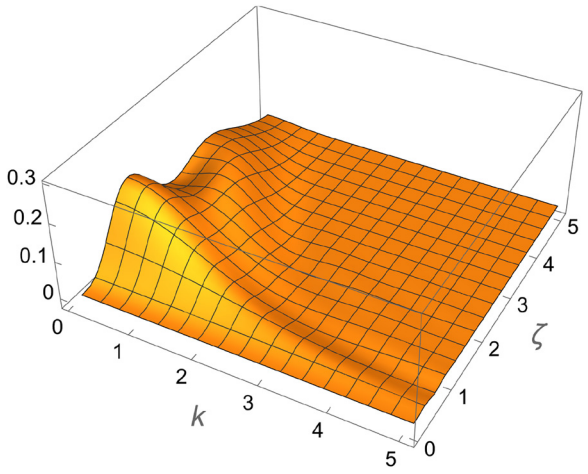

Figure 9: Wigner function of superposition of ground state and first excited state for non-time-resolving measurement $p_1 W(\zeta, k, a_1) + p_2 W(\zeta, k, a_2)$, see Eq. (27), with $p_1 = 0.7$ and $p_2 = 0.3$.

$$
\begin{aligned}
|F_{\mathrm{s}}(k,t)|^2 = {} & p_1|F(k,a_1)|^2 + p_2|F(k,a_2)|^2 + 2\sqrt{p_1 p_2} \\
& \times \left\{ \cos\left[\frac{E_1 - E_2}{\hbar} t\right] \left[f_{\mathrm{c}}(k,a_1) f_{\mathrm{c}}(k,a_2) \right.\right. \\
& \left. + f_{\mathrm{s}}(k,a_1) f_{\mathrm{s}}(k,a_2) \right] \\
& - \sin\left[\frac{E_1 - E_2}{\hbar} t\right] \left[f_{\mathrm{s}}(k,a_1) f_{\mathrm{c}}(k,a_2) \right. \\
& \left.\left. - f_{\mathrm{c}}(k,a_1) f_{\mathrm{s}}(k,a_2) \right] \right\}. \qquad (26)
\end{aligned}
$$

The time dependence of this momentum spectrum could also be measured experimentally.

Figure 7(b) gives an example of Eq. (26) with $p_1 = 0.7$ and $p_2 = 0.3$. If we chose $p_1 = 1$ and $p_2 = 0$, or $p_1 = 0$ and $p_2 = 1$, we would instead recover Figure 2(b). In the case of a non-time-resolving measurement, we have to integrate time t in Eq. (26) over one time period. Hence, the interference term disappears and we obtain only the first two terms $p_1|F(k,a_1)|^2 + p_2|F(k,a_2)|^2$, which, using $p_1 = 0.7$ and $p_2 = 0.3$, is the function in blue in Figure 6.

Using Eqs. (16) and (20), the Wigner function of the coherent superposition can be found to be

$$
\begin{aligned}
W_{\mathrm{s}}(\zeta,k,t) = {} & p_1 W(\zeta,k,a_1) + p_2 W(\zeta,k,a_2) \\
& + \sqrt{p_1 p_2}\frac{1}{\pi}\int_{-\infty}^{\infty} \mathrm{Ai}\left(\zeta - \frac{\zeta'}{2} + a_2\right) \\
& \times \mathrm{Ai}\left(\zeta + \frac{\zeta'}{2} + a_1\right) \Theta\left(\zeta - \frac{\zeta'}{2}\right) \\
& \times \Theta\left(\zeta + \frac{\zeta'}{2}\right) \cos\left(\frac{E_1 - E_2}{\hbar} t + \zeta' k\right) \mathrm{d}\zeta'. \\
& \qquad (27)
\end{aligned}
$$

The single Wigner functions $W(\zeta,k,a_1)$ and $W(\zeta,k,a_2)$ have already been depicted in Figure 5(a) and (b), respectively, while the integral on the right-hand side of Eq. (27), the interference term, can be evaluated similarly to Eq. (19).

If the time t cannot be resolved experimentally, we have to integrate over one time period, which causes the interference term to disappear. The resulting Wigner function for an example population is given in Figure 9.

3 Wave function in a double mirror system (region I)

In a real experiment ultracold neutrons (UCNs) are induced in a double mirror system Figure 10 (region *I*), [23]. The situation is significantly different from Section 2. Because of the 2 mirrors there are 2 boundary conditions where the wave function has to be zero. This entails a linear combination of the two Airy-functions Ai(z) and Bi(z) and modified eigenvalues. In this section we will record the position-dependent wave function as well as the Fourier transform. At the end of the section the Wigner function is calculated and graphically displayed. It turns out that – because of the rough upper mirror – essentially the ground state survives at the end of double-mirror system.

Well, in this chapter we are considering the experimental setting depicted in Figure 10, and focus on the states in region I. We can take the normalized wave function of

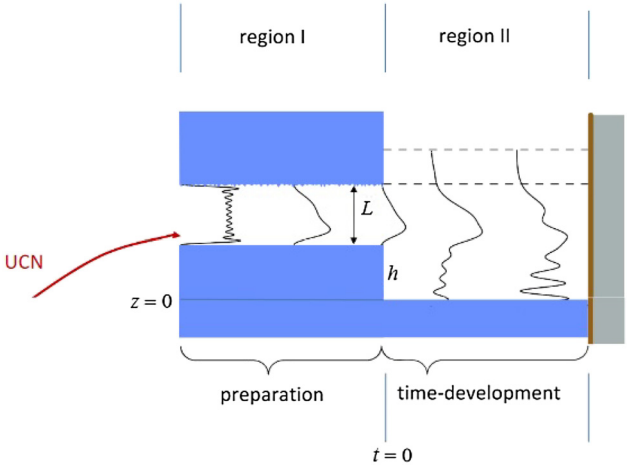

Figure 10: Sketch of the two regions I and II, in which the horizontal direction (abscissa) is the time t-axis and the vertical direction (ordinate) is the z–axis. UCN (ultracold neutrons) enter a double mirror system of distance L, called the preparation region (or region I). The lower mirror is smooth, the upper one rough. Due to the roughness of the upper mirror, at the end of region I, only the ground state of the quantum wave is left ($m = 1$). In region II, the quantum wave falls down a step of height h onto a smooth mirror located at $z = 0$. The transition point from region I to II is where we choose to set $t = 0$. At the end of region II, a track detector measures the vertical space distribution $|\psi_{m,\mathrm{II}}(z,t)|^2$.

the qBOUNCE problem in the case of two mirrors with fixed separation L from article [32] Eq. (10):

$$\begin{aligned}
\psi_m^{(0)}(z,t) &= \frac{1}{\sqrt{z_0}}\frac{1}{N_m}\mathrm{e}^{-\frac{\mathrm{i}}{\hbar}\bar{E}_m t}\left[b_m \mathrm{Ai}\left(\frac{z-\bar{z}_m}{z_0}\right)\right.\\
&\quad \left. - a_m \mathrm{Bi}\left(\frac{z-\bar{z}_m}{z_0}\right)\right],\\
N_m^2 &= \left[b_m \mathrm{Ai}'\left(\frac{-\bar{z}_m}{z_0}\right) - a_m \mathrm{Bi}'\left(\frac{-\bar{z}_m}{z_0}\right)\right]^2\\
&\quad - \left[b_m \mathrm{Ai}'\left(\frac{L-\bar{z}_m}{z_0}\right) - a_m \mathrm{Bi}'\left(\frac{L-\bar{z}_m}{z_0}\right)\right]^2,\\
a_m &= \mathrm{Ai}\left(\frac{-\bar{z}_m}{z_0}\right), \quad b_m = \mathrm{Bi}\left(\frac{-\bar{z}_m}{z_0}\right).
\end{aligned} \tag{28}$$

Here the prime denotes derivatives with respect to the argument, i.e., $z_0\,\mathrm{d}/\mathrm{d}z$, and $\mathrm{Ai}(x)$ and $\mathrm{Bi}(x)$ are the two independent solutions of Airy's equation. Due to the experimental setting, we assume that the wave function in region I has support only on $[0, L] \times (-\infty, 0]$, but we keep this assumption implicit for notational convenience. Below we present a selection of possible numerical values for the parameters used in Eq. (28):

$$\begin{aligned}
&L = 28\,\mu\mathrm{m},\\
&m = 1, \quad \bar{E}_1 \approx 1.40821\,\mathrm{peV}, \quad \bar{z}_1 \approx 13.73133\,\mu\mathrm{m},\\
&m = 2, \quad \bar{E}_2 \approx 2.53045\,\mathrm{peV}, \quad \bar{z}_2 \approx 24.67419\,\mu\mathrm{m},\\
&m = 3, \quad \bar{E}_3 \approx 3.84125\,\mathrm{peV}, \quad \bar{z}_3 \approx 37.45569\,\mu\mathrm{m},\\
&m = 4, \quad \bar{E}_4 \approx 5.64658\,\mathrm{peV}, \quad \bar{z}_4 \approx 55.05930\,\mu\mathrm{m},\\
&m = 5, \quad \bar{E}_5 \approx 7.98191\,\mathrm{peV}, \quad \bar{z}_5 \approx 77.83089\,\mu\mathrm{m},\\
&m = 6, \quad \bar{E}_6 \approx 10.8441\,\mathrm{peV}, \quad \bar{z}_6 \approx 105.7399\,\mu\mathrm{m}.
\end{aligned} \tag{29}$$

Here we have $\bar{E}_m = \bar{z}_m m_\mathrm{N} g$. The energy spectrum $\bar{E}_m$ is obtained by the conditions that the wave functions vanish at the lower as well as upper mirror surface, i.e., $\psi_m^{(0)}(0) = \psi_m^{(0)}(L) = 0$.

3.1 Fourier transformation of the wave function

The Fourier transformation of the wave function in Eq. (29) is given by

$$\begin{aligned}
F_m^{(0)}(k,t) &= \frac{1}{\sqrt{2\pi}}\int_{-\infty}^{\infty} \mathrm{e}^{-\mathrm{i}kz}\psi_m^{(0)}(z,t)\,\mathrm{d}z\\
&= C_m(t)\int_0^L \mathrm{e}^{-\mathrm{i}kz}\left[b_m \mathrm{Ai}\left(\frac{z-\bar{z}_m}{z_0}\right)\right.\\
&\quad \left. - a_m \mathrm{Bi}\left(\frac{z-\bar{z}_m}{z_0}\right)\right]\mathrm{d}z,
\end{aligned} \tag{30}$$

where $C_m(t) = \frac{1}{\sqrt{2\pi}\sqrt{z_0}N_m}\mathrm{e}^{-\frac{\mathrm{i}}{\hbar}\bar{E}_m t}$ and we made use of the restrictions on the support of the wave function that we mentioned earlier. Since z has the dimension of a length, here the variable k must have the dimension of an inverse length and is related to the physical momentum k_p by

$$k = \frac{k_\mathrm{p}}{\hbar}. \tag{31}$$

We define the following stationary quantities:

$$\begin{aligned}
\alpha_\mathrm{c}(k,m) &:= \frac{1}{C_m(t)}\mathrm{Re}\left[F_m^{(0)}(k,t)\right],\\
\alpha_\mathrm{s}(k,m) &:= -\frac{1}{C_m(t)}\mathrm{Im}\left[F_m^{(0)}(k,t)\right],
\end{aligned} \tag{32}$$

such that

$$F_m^{(0)}(k,t) = C_m(t)\left[\,\alpha_\mathrm{c}(k,m) - \mathrm{i}\alpha_\mathrm{s}(k,m)\,\right], \tag{33}$$

and the spectral function is given through

$$|F_m^{(0)}(k)|^2 = |C_m|^2 \left[\alpha_c^2(k,m) + \alpha_s^2(k,m) \right] \tag{34}$$

with $|C_m|^2 = \frac{1}{2\pi z_0 N_m^2}$. Notice that this momentum distribution is stationary. It is depicted for the cases $m = 1$, $m = 2$, and $m = 3$ in Figure 11(a)–(c), respectively. These figures also explicitly show the respective $|C_m|^2\alpha_s^2(k,m)$ and $|C_m|^2\alpha_c^2(k,m)$.

The wave function for two mirrors $\psi_m^{(0)}(z,t)$ in Eq. (28) is normalized as

$$\int_{-\infty}^{\infty} |\psi_m^{(0)}(z,t)|^2 \, \mathrm{d}z = \int_0^L |\psi_m^{(0)}(z,t)|^2 \, \mathrm{d}z = 1. \tag{35}$$

In a similar way, the spectral function $|F_m^{(0)}(k)|^2$ has to be normalized, such that

$$\int_{-\infty}^{\infty} |F_m^{(0)}(k)|^2 \, \mathrm{d}k = 1. \tag{36}$$

We can easily show that this normalization is indeed valid here by using the first equality in Eq. (30):

$$\begin{aligned}
&\int_{-\infty}^{\infty} |F_m^{(0)}(k,t)|^2 \mathrm{d}k \\
&\quad = \frac{1}{2\pi} \int_{-\infty}^{\infty} \mathrm{e}^{\mathrm{i}kz'} \psi_m^{(0)*}(z',t) \mathrm{e}^{-\mathrm{i}kz} \psi_m^{(0)}(z,t) \, \mathrm{d}z' \mathrm{d}z \mathrm{d}k \\
&\quad = \int_{-\infty}^{\infty} \delta(z-z') \psi_m^{(0)*}(z',t) \psi_m^{(0)}(z,t) \, \mathrm{d}z' \mathrm{d}z \\
&\quad = \int_{-\infty}^{\infty} |\psi_m^{(0)}(z,t)|^2 \, \mathrm{d}z \\
&\quad = 1.
\end{aligned} \tag{37}$$

3.2 Wigner function

Using Eq. (28) with Eq. (15) gives the Wigner function

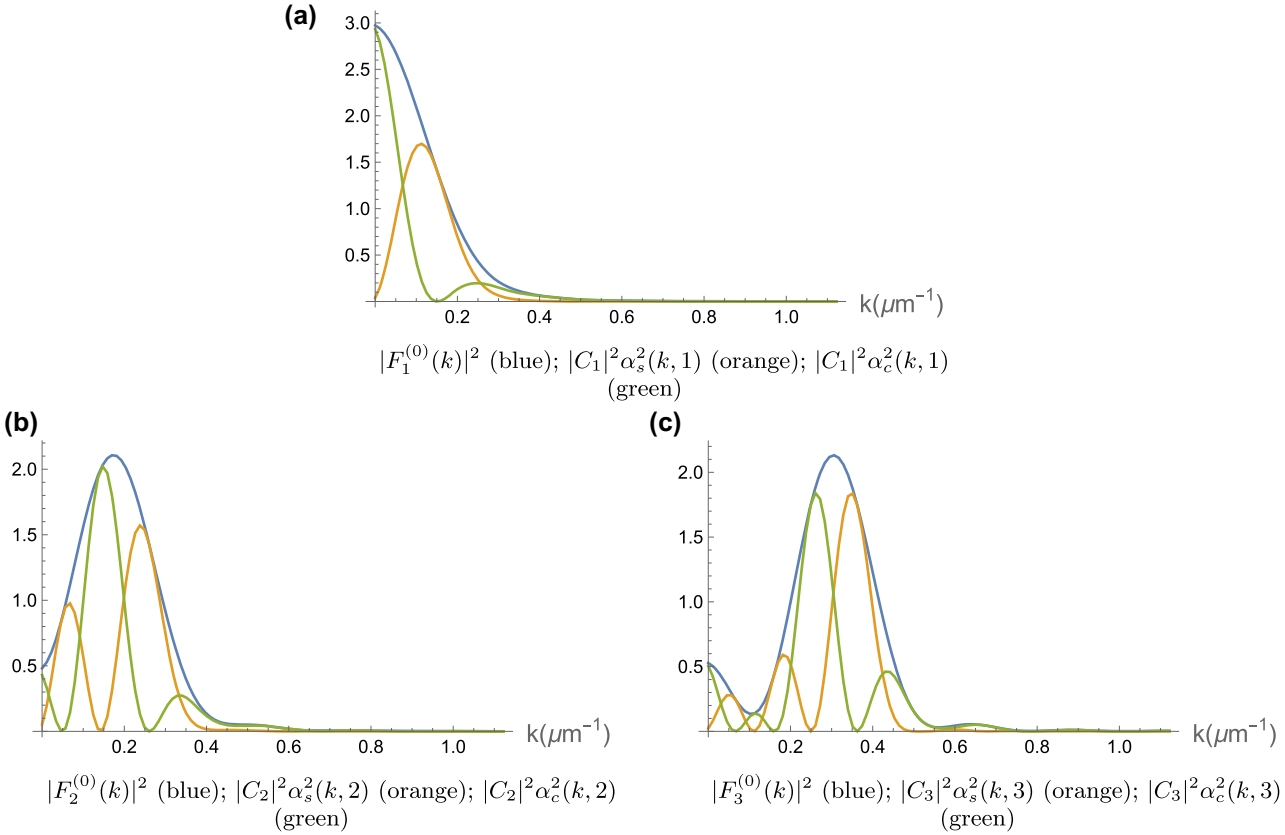

$|F_1^{(0)}(k)|^2$ (blue); $|C_1|^2\alpha_s^2(k,1)$ (orange); $|C_1|^2\alpha_c^2(k,1)$ (green)

$|F_2^{(0)}(k)|^2$ (blue); $|C_2|^2\alpha_s^2(k,2)$ (orange); $|C_2|^2\alpha_c^2(k,2)$ (green)

$|F_3^{(0)}(k)|^2$ (blue); $|C_3|^2\alpha_s^2(k,3)$ (orange); $|C_3|^2\alpha_c^2(k,3)$ (green)

Figure 11: Spectral functions of the ground state, and first and second excited state, see Eq. (34).

$$W_m^{(0)}(z,k) = \frac{1}{2\pi}\int_{-\infty}^{\infty} \mathrm{e}^{\mathrm{i}z'k}\psi_m^{(0)*}\left(z+\frac{z'}{2},t\right)\psi_m^{(0)} \times\left(z-\frac{z'}{2},t\right)\mathrm{d}z' = \frac{1}{2\pi z_0 N_m^2}\int_{A(z)}^{B(z)} \mathrm{e}^{\mathrm{i}z'k} D(z,z')\,\mathrm{d}z' \tag{38}$$

with

$$D(z,z') := \left[b_m \mathrm{Ai}\left(\frac{z+\frac{z'}{2}-\bar{z}_m}{z_0}\right) - a_m \mathrm{Bi}\left(\frac{z+\frac{z'}{2}-\bar{z}_m}{z_0}\right)\right] \times\left[b_m \mathrm{Ai}\left(\frac{z-\frac{z'}{2}-\bar{z}_m}{z_0}\right) - a_m \mathrm{Bi}\left(\frac{z-\frac{z'}{2}-\bar{z}_m}{z_0}\right)\right], \tag{39}$$

and $A(z)$ and $B(z)$ are the limits of integration that appear due to the restrictions on the support of $\psi_m^{(0)}$. It can directly be seen that $D(z,z') = D(z,-z')$.

We will now determine the limits of integration. For this, we consider that z is limited between 0 and L, leading us to the following 4 equations

$$\begin{aligned} &z+\frac{z'}{2}=0 \;\Rightarrow\; z'=-2z; \quad z-\frac{z'}{2}=0 \;\Rightarrow\; z'=2z;\\ &z+\frac{z'}{2}=L \;\Rightarrow\; z'=2(L-z);\\ &z-\frac{z'}{2}=L \;\Rightarrow\; z'=2(z-L); \end{aligned} \tag{40}$$

which represent 4 straight lines in the (z,z')-diagram and generate a rhombus. The values inside of this rhombus are the allowed values for integration. Therefore, we conclude

$$\begin{aligned} &0\le z\le\frac{L}{2} \;\Rightarrow\; A(z) = -2z \le z' \le 2z = B(z);\\ &\frac{L}{2}\le z\le L \;\Rightarrow\; A(z) = -2(L-z) \le z' \le 2(L-z) = B(z). \end{aligned} \tag{41}$$

Since $A(z) = -B(z)$, the Wigner function can finally be written as

$$W_m^{(0)}(z,k) = \frac{1}{\pi z_0 N_m^2}\int_0^{B(z)} \cos(z'k)D(z,z')\,\mathrm{d}z' = \frac{1}{\pi z_0 N_m^2}\begin{cases} \int_0^{2z} \cos(z'k)D(z,z')\,\mathrm{d}z', & \text{for } 0<z<\frac{L}{2} \\ \int_0^{2(L-z)} \cos(z'k)D(z,z')\,\mathrm{d}z', & \text{for } \frac{L}{2}<z<L \end{cases}. \tag{42}$$

It is depicted in Figure 12(a)–(c) for $m=1$, $m=2$, and $m=3$, respectively. As can be seen from Figure 12(a), the Wigner function $W_1^{(0)}(z,k)$ of the ground state ($m=1$) is positive everywhere. This is not the case for the Wigner function $W_2^{(0)}(z,k)$ of the first excited state ($m=2$), see Figure 12(b), and the Wigner function $W_3^{(0)}(z,k)$ of the second excited state ($m=3$), see Figure 12(c). For these states we can clearly observe negative regions of the Wigner functions. This is a very characteristic property of excited states in quantum mechanics. At $z=0$ (bottom mirror) and at $z=28$ µm (top mirror) the Wigner functions vanish exactly because of the boundary conditions.

In summary, in this chapter, we considered the eigenstates of the neutron wave function in a double mirror system, calculated the spectral functions and evaluated the corresponding Wigner functions. The latter enabled us to look into the complete phase space in order to study momentum and position simultaneously.

4 "Free fall" of wave function after double mirror (region II)

Here we shall discuss an entire new physical problem. Because of Earth's gravitational force the quantum wave, coming out from the double mirror system of region I, freely falls down a step of height h, see Figure 10. This region will be called region II. In this region only 1 smooth mirror lies at the bottom and above there is no more mirror. Considered classically, the particle would periodically fall down, impinge on the mirror being reflected like a bouncing ball. Due to the quantum character of this qBounce arrangement with one mirror only the quantum waves are superpositions of eigenstates with different energies E_n. Interference of the corresponding time-dependent wavefunctions has to be expected. Subsequently we investigate

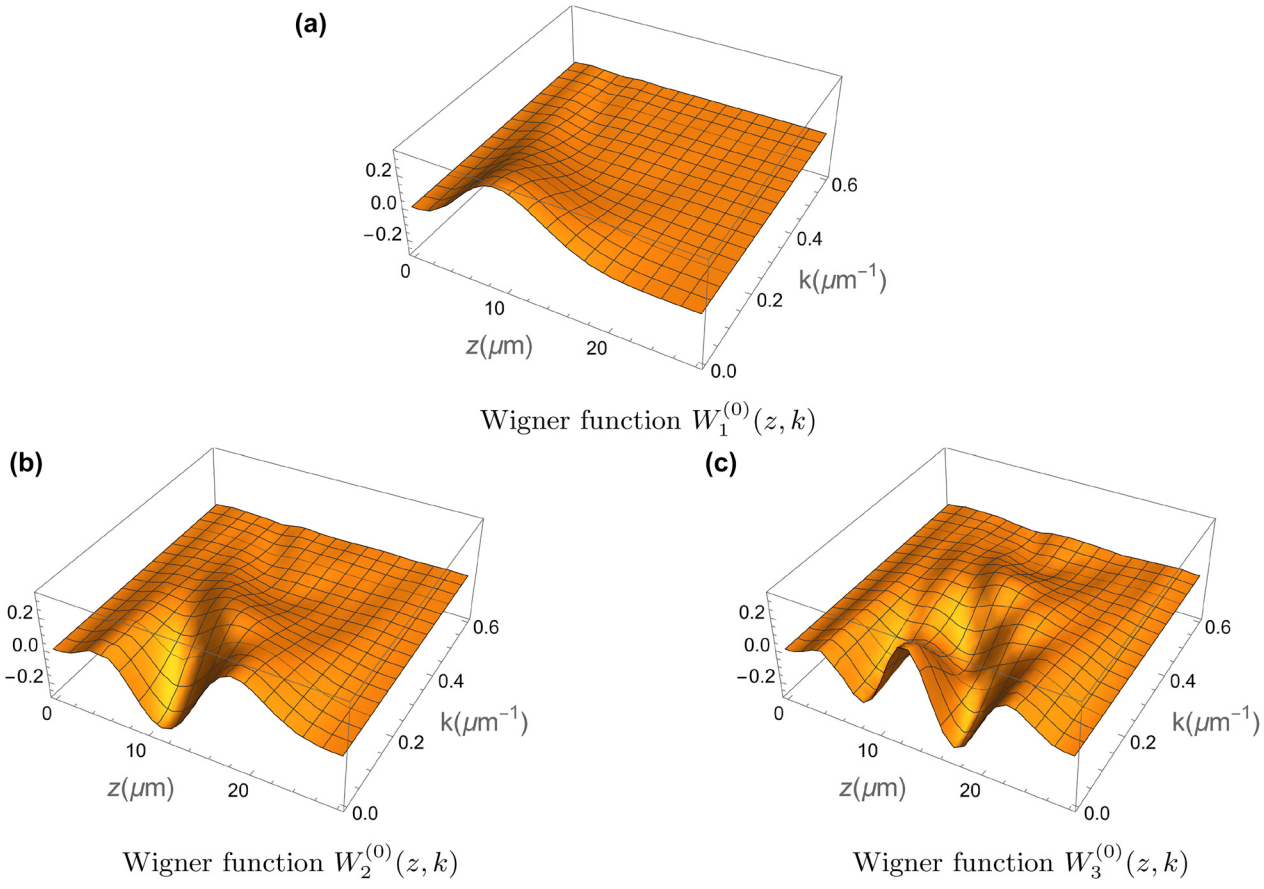

Figure 12: Wigner functions of the ground state, and first and second excited state, see Eq. (42).

the time-dependent spatial and momentum distribution functions for various initial states. At the end of this chapter we study the Wigner functions.

Therefore, in this chapter we consider the "free fall" of a wave function which exits a double mirror system (we denote this region by I, see Figure 10). The wave function reaches a second region II, where it falls down a height $h = 27$ μm on a subsequent static mirror located below the double mirror system. This case has been investigated theoretically in [30]. The wave function in region I has been given in Eq. (28). Since we are now also going to consider region II, and for convenience, we apply the coordinate shift $z \to z - h$ to the result from Eq. (28), such that we have

$$\psi_{m,\mathrm{I}}(z,t) := \bar{C}_m \mathrm{e}^{-\frac{\mathrm{i}}{\hbar}\bar{E}_m t}\left[b_m \mathrm{Ai}\left(\frac{z-h-\bar{z}_m}{z_0}\right) - a_m \mathrm{Bi}\left(\frac{z-h-\bar{z}_m}{z_0}\right)\right], \tag{43}$$

where we introduced the notation $\bar{C}_m := \frac{1}{\sqrt{z_0}N_m}$, and the wave function has support only on $[h, L+h] \times (-\infty, 0]$.

In region II the wave function takes on the following form

$$\psi_{m,\mathrm{II}}(z,t) = \bar{C}_m \sum_{n=1}^{\infty} D_{n,m} \mathrm{Ai}\left(\frac{z-z_n}{z_0}\right) \mathrm{e}^{-\frac{\mathrm{i}}{\hbar}E_n t} \tag{44}$$

and includes coefficients

$$\begin{aligned} D_{n,m} := \Bigg\{ & \left[b_m \mathrm{Ai}'\left(\frac{L-\bar{z}_m}{z_0}\right) - a_m \mathrm{Bi}'\left(\frac{L-\bar{z}_m}{z_0}\right)\right] \\ & \times \left[\mathrm{Ai}\left(\frac{L+h-z_n}{z_0}\right) - \mathrm{Ai}\left(\frac{L-\bar{z}_m}{z_0}\right)\right] \\ & - \left[b_m \mathrm{Ai}'\left(-\frac{\bar{z}_m}{z_0}\right) - a_m \mathrm{Bi}'\left(-\frac{\bar{z}_m}{z_0}\right)\right] \\ & \times \left[\mathrm{Ai}\left(\frac{h-z_n}{z_0}\right) - a_m\right] \Bigg\} \left(\frac{z_0}{z_n - \bar{z}_m - h}\right) \\ & \times \left[\mathrm{Ai}'\left(-\frac{z_n}{z_0}\right)\right]^{-2}. \end{aligned} \tag{45}$$

Formula Eq. (44) together with Eq. (45) corresponds exactly to Eq. (70) in article [30].

The wave function in region II, given in Eq. (44), should have support only on $[0,\infty)\times(0,\infty)\cup[h,L+h]\times\{0\}$. This results from the requirement of a continuous transition between regions I and II expressed by

$$\psi_{m,\mathrm{I}}(z,t=0)=\psi_{m,\mathrm{II}}(z,t=0), \tag{46}$$

which can only be fulfilled if both $\psi_{m,\mathrm{I}}(z,t)$ and $\psi_{m,\mathrm{II}}(z,t)$ have the same support at $t=0$.

Next, we examine the coefficients $D_{n,m}$ for $m=1,2$ and $n=1,2,\ldots$ For this, in what follows, we present the numerical values of a few selected parameters relevant for Eq. (45):

$$\begin{aligned} z_1&=13.71680\,\mu\mathrm{m}, & z_2&=23.98246\,\mu\mathrm{m},\\ z_3&=32.38707\,\mu\mathrm{m}, & z_4&=39.81502\,\mu\mathrm{m},\\ z_5&=46.60526\,\mu\mathrm{m}, & z_6&=52.93243\,\mu\mathrm{m},\\ z_7&=58.90210\,\mu\mathrm{m}, & z_8&=64.58300\,\mu\mathrm{m},\\ z_9&=70.02430\,\mu\mathrm{m}, & z_{10}&=75.26180\,\mu\mathrm{m},\\ z_{11}&=80.23200\,\mu\mathrm{m}, & z_{12}&=85.22950\,\mu\mathrm{m}. \end{aligned} \tag{47}$$

Figure 13 shows some of the first coefficients $D_{n,m}$ for the cases $m=1$ and $m=2$. From there it can be seen that for $n>12$ the coefficients $D_{n,m}$ become very small and can therefore be neglected.

Now we can check whether $\psi_{1,\mathrm{I}}(z,t=0)$ and $\psi_{1,\mathrm{II}}(z,t=0)$ fulfill the condition in Eq. (46). We do this for the ground state $m=1$. For this, we consider only a finite number of coefficients $D_{n,1}$. The results including n up to 12 and 15 are presented in Figures 14(a) and (b), respectively. There the abscissa represents the $z-$coordinate in µm shifted to the point of origin of the coordinate system. Therefore, in region I there are values of z from 0 to L. The agreement between $\psi_{1,\mathrm{I}}(z,t=0)$ and the plotted approximation of $\psi_{1,\mathrm{II}}(z,t=0)$ is very good except near certain regions, e.g., around $z=0$. These small differences supposedly are due to using only a finite number of $D_{n,1}$-coefficients. We expect the differences to become smaller when more $D_{n,1}$-coefficients are considered.

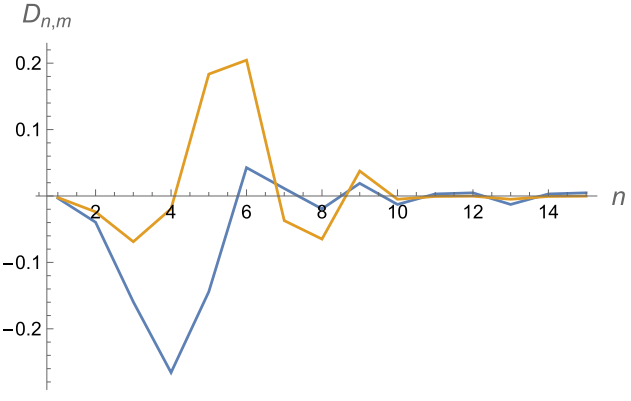

Figure 13: Coefficients $D_{n,m}$ from Eq. (45) for ground state with $m=1$ (blue) and first excited state with $m=2$ (orange); for these cases, the coefficients are very small for $n>12$.

4.1 Spatial distribution (SD) in "free-fall" region

The spatial distribution in region II follows from Eq. (44):

$$|\psi_{m,\mathrm{II}}(z,t)|^2=\left|\bar{C}_m\sum_{n=1}^{\infty}D_{n,m}\mathrm{Ai}\left(\frac{z-z_n}{z_0}\right)\mathrm{e}^{-\frac{\mathrm{i}}{\hbar}E_n t}\right|^2. \tag{48}$$

We define

$$\begin{aligned} G_m^c(z,t)&:=\bar{C}_m\sum_{n=1}^{\infty}D_{n,m}\mathrm{Ai}\left(\frac{z-z_n}{z_0}\right)\cos\left(\frac{E_n}{\hbar}t\right),\\ G_m^s(z,t)&:=\bar{C}_m\sum_{n=1}^{\infty}D_{n,m}\mathrm{Ai}\left(\frac{z-z_n}{z_0}\right)\sin\left(\frac{E_n}{\hbar}t\right), \end{aligned} \tag{49}$$

such that the spatial distribution in region II reads

$$|\psi_{m,\mathrm{II}}(z,t)|^2=\left[G_m^c(z,t)\right]^2+\left[G_m^s(z,t)\right]^2. \tag{50}$$

Whenever performing numerical calculations we will only consider the sums in Eq. (49) from $n=1$ to 15 due to the smallness of later coefficients $D_{n,m}$.

In Figure 15(a) and (b) the spatial distributions (SD) $|\psi_{1,\mathrm{II}}(z,t)|^2$ and $|\psi_{2,\mathrm{II}}(z,t)|^2$, respectively, are plotted as a function of the $z-$coordinate (in µm) and time t (in s). For $t=0$ the ground and the first excited state are visible. This means, that between $z=0$ and $z=h=27$ µm the SD are zero. Between $z=h$ and $z=h+L=55$ µm the SD have the shape of the ground state, see Figure 15(a), or the first excited state, Figure 15(b). For $z>55$ µm the SD vanish again. While t evolves, the wave function is reflected from the mirror in region II multiple times. Since the frequencies $E_n/\hbar$ vary during this process, which leads to varying superpositions of waves, more complicated SD pictures result at times after $t=0$.

Figure 16(a) and (b) show the cosine and sine distribution functions $|G_1^c(z,t)|^2$ and $|G_1^s(z,t)|^2$ of the ground state. The sum of these functions yields Figure 15(a). It is interesting to consider these parts of $|\psi_{1,\mathrm{II}}(z,t)|^2$ separately since they could be important for interpreting experimental results.

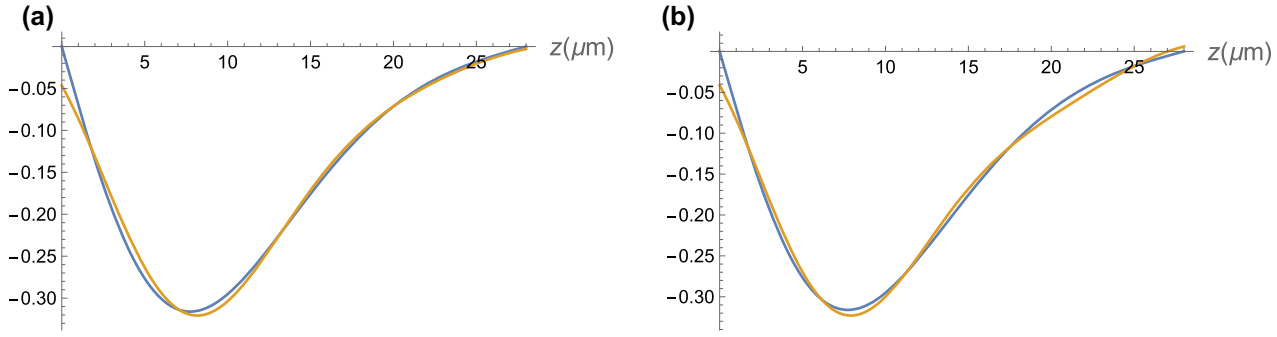

Using only coefficients $D_{n,1}$ for $n = 1$ to $n = 12$, the agreement is already considerable.

Using only coefficients $D_{n,1}$ for $n = 1$ to $n = 15$

Figure 14: Comparison of $\psi_{1,\mathrm{I}}(z, t = 0)$ (blue) with $\psi_{1,\mathrm{II}}(z, t = 0)$ (orange) for $m = 1$, see Eq. (46); the coordinate $z = h$ has been shifted to the point of origin.

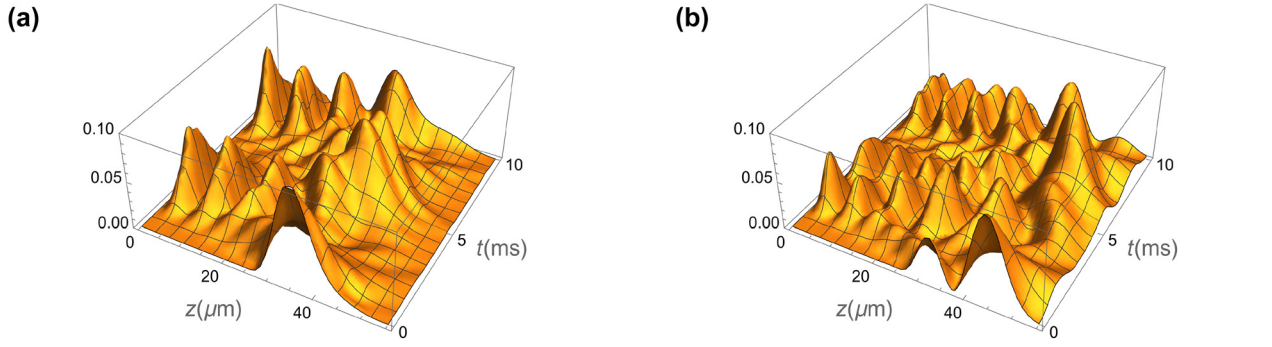

Spatial distribution $|\psi_{1,\mathrm{II}}(z, t)|^2$; The ground state $(m = 1)$ appears at $t = 0$. The density distribution peaks nicely along the classical parabola.

Spatial distribution $|\psi_{2,\mathrm{II}}(z, t)|^2$; The first excited state $(m = 2)$ appears at $t = 0$.

Figure 15: Spatial distributions, see Eq. (50), in region II.

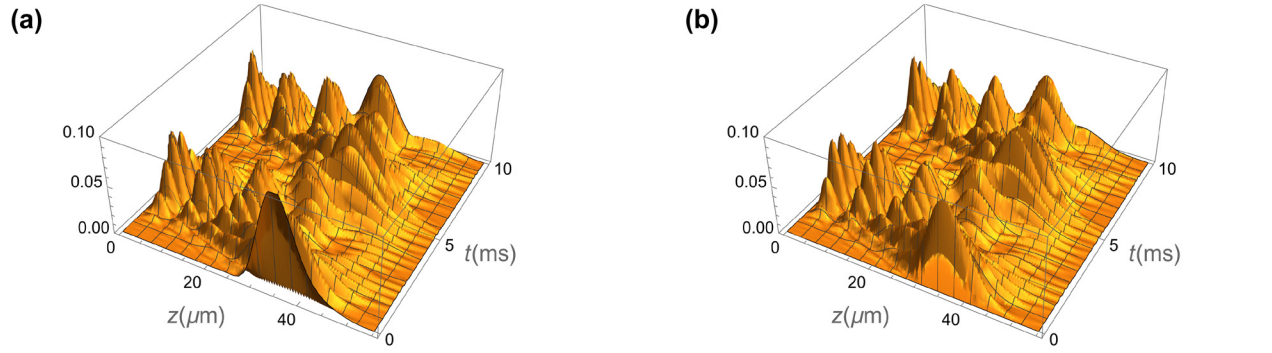

Cosine spatial distribution $|G^c_m(z, t)|^2$; The ground state $(m = 1)$ appears at $t = 0$.

Sine spatial distribution $|G^s_m(z, t)|^2$; The ground state $(m = 1)$ appears at $t = 0$.

Figure 16: Trigonometric spatial distributions, see Eq. (50), in region II.

4.2 Spatial distribution of mixtures

So far, we have considered only a particular state (ground state or first excited state) which enters region II. It would be interesting to consider, for example, a mixture of these two types of quantum states arriving at the step before entering region II. This case will now be investigated. In the following, we distinguish between coherent mixtures and

incoherent mixtures. We consider mixtures of the ground state with the first excited state.

4.2.1 Coherent mixtures

In the beginning, we look at the following coherent superposition state:

$$\psi_{1+2,\mathrm{II}}(z,t) = \sqrt{p_1}\,\psi_{1,\mathrm{II}}(z,t) + \sqrt{p_2}\,\psi_{2,\mathrm{II}}(z,t), \tag{51}$$

where p_1 and p_2 are probabilities, and we ignore a potential phase between both terms for simplicity. Note that

$$\int_0^\infty |\psi_{1+2,\mathrm{II}}(z,t)|^2\,\mathrm{d}z = 1 \tag{52}$$

because of the orthonormality of the eigenfunctions: $\int_0^\infty \psi_1\psi_2\,\mathrm{d}z = 0$.

The next step is to calculate the spatial distribution of the coherent superposition $|\psi_{1+2,\mathrm{II}}(z,t)|^2$. This can be accomplished by using Eq. (44) for $m = 1$ and $m = 2$:

$$\begin{aligned}\psi_{1+2,\mathrm{II}}(z,t) &= \sqrt{p_1}\,\bar{C}_1\sum_{n=1}^{\infty} D_{n,1}\mathrm{Ai}\left(\frac{z-z_n}{z_0}\right)\mathrm{e}^{-\mathrm{i}\frac{E_n}{\hbar}t}\\ &\quad+\sqrt{p_2}\,\bar{C}_2\sum_{n=1}^{\infty} D_{n,2}\mathrm{Ai}\left(\frac{z-z_n}{z_0}\right)\mathrm{e}^{-\mathrm{i}\frac{E_n}{\hbar}t}\\ &= \sum_{n=1}^{\infty}\mathrm{Ai}\left(\frac{z-z_n}{z_0}\right)\left(\sqrt{p_1}\,\bar{C}_1D_{n,1}+\sqrt{p_2}\,\bar{C}_2D_{n,2}\right)\\ &\quad\times\left[\cos\left(\frac{E_n}{\hbar}t\right)-\mathrm{i}\,\sin\left(\frac{E_n}{\hbar}t\right)\right].\end{aligned} \tag{53}$$

For numerical calculations we will again cut off the infinite sums at $n = 15$. We define:

$$\begin{aligned}|\psi_{1+2,\mathrm{II}}(z,t)|^2 &= \left[H^{\mathrm{c}}_{1+2}(z,t)\right]^2+\left[H^{\mathrm{s}}_{1+2}(z,t)\right]^2,\\ H^{\mathrm{c}}_{1+2}(z,t) &:= \sum_{n=1}^{\infty}\mathrm{Ai}\left(\frac{z-z_n}{z_0}\right)\left(\sqrt{p_1}\,\bar{C}_1D_{n,1}\right.\\ &\quad\left.+\sqrt{p_2}\,\bar{C}_2D_{n,2}\right)\cos\left(\frac{E_n}{\hbar}t\right),\\ H^{\mathrm{s}}_{1+2}(z,t) &:= \sum_{n=1}^{\infty}\mathrm{Ai}\left(\frac{z-z_n}{z_0}\right)\left(\sqrt{p_1}\,\bar{C}_1D_{n,1}\right.\\ &\quad\left.+\sqrt{p_2}\,\bar{C}_2D_{n,2}\right)\sin\left(\frac{E_n}{\hbar}t\right).\end{aligned} \tag{54}$$

In Figure 17(a) and (b) we present two examples, for which the coherent superposition of mixtures can be observed, namely for $p_1 = 0.7$ and $p_2 = 0.3$, and $p_1 = 0.5$ and $p_2 = 0.5$, respectively. Because of the superposition of waves in Eq. (51), in both cases, only the ground state has been amplified at $t = 0$. Altogether, we conclude that using a coherent superposition is not very useful for obtaining a damped behavior of the oscillations. We expect this to be different when using incoherent mixtures.

4.2.2 Incoherent mixtures

Incoherent mixtures can be described by the following formula:

$$|\psi^{\mathrm{incoh}}_{\mathrm{mix,II}}(z,t)|^2 = p_1|\psi_{1,\mathrm{II}}(z,t)|^2 + p_2|\psi_{2,\mathrm{II}}(z,t)|^2. \tag{55}$$

In Figure 18(a) and (b) two examples are presented, for which incoherent mixtures can be observed, namely

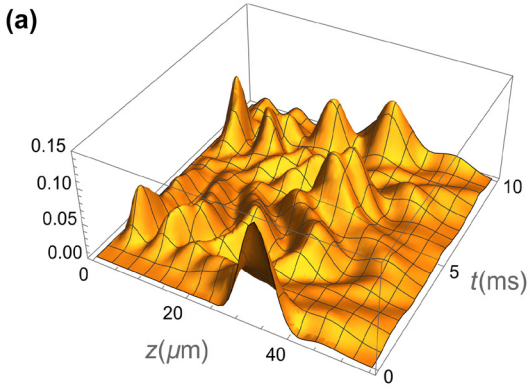

Coherent mixture $|\psi_{1+2,\mathrm{II}}(z,t)|^2$ with $p_1 = 0.7$ and $p_2 = 0.3$

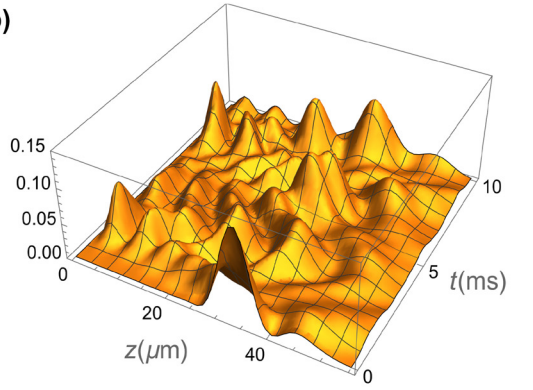

Coherent mixture $|\psi_{1+2,\mathrm{II}}(z,t)|^2$ with $p_1 = p_2 = 0.5$

Figure 17: Coherent mixtures, see Eq. (54), in region II.

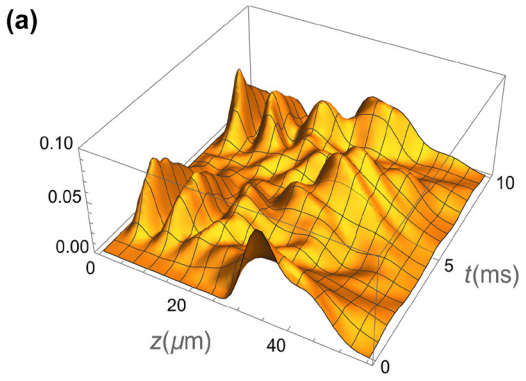

Incoherent mixture $|\psi^{\text{incoh}}_{\text{mix,II}}(z,t)|^2$ with $p_1 = 0.7$ and $p_2 = 0.3$

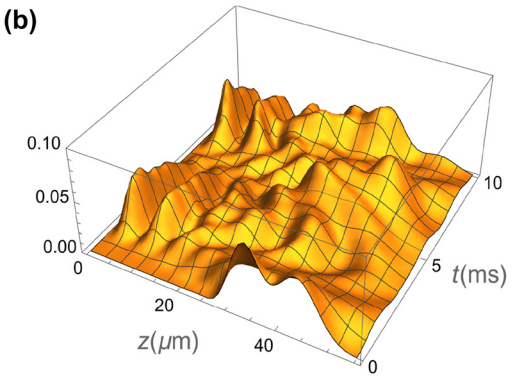

Incoherent mixture $|\psi^{\text{incoh}}_{\text{mix,II}}(z,t)|^2$ with $p_1 = p_2 = 0.5$

Figure 18: Incoherent mixtures, see Eq. (55), in region II.

for $p_1 = 0.7$ and $p_2 = 0.3$, and $p_1 = 0.5$ and $p_2 = 0.5$, respectively. In Figure 18(a), for example, at $t = 0$ the shape of the SD is qualitatively the same as in Figure 8. Altogether, the oscillations are less distinct than in the previous case.

Figure 19(a) and (b) show two examples, in which $|\psi^{\text{incoh}}_{\text{mix,II}}(z,t)|^2$ is separated into a cosine and a sine part. The formulas are included in the corresponding figure captions, and the sum of both of these plots gives the result in Figure 18(a).

4.3 Momentum distribution

The momentum distribution in region II is calculated through a Fourier transformation:

$$
\begin{aligned}
|F_{m,\text{II}}(k,t)|^2 &= \left| \frac{1}{\sqrt{2\pi}} \int_{-\infty}^{\infty} \mathrm{e}^{-\mathrm{i}kz} \psi_{m,\text{II}}(z,t)\, \mathrm{d}z \right|^2 \\
&= \left| \frac{1}{\sqrt{2\pi}} \bar{C}_m \sum_{n=1}^{\infty} D_{n,m} \mathrm{e}^{-\frac{i}{\hbar}E_n t} \right. \\
&\qquad \left. \times \left[f^{\text{Ai}}_{\text{c,II}}(k,n) - i\, f^{\text{Ai}}_{\text{s,II}}(k,n) \right] \right|^2 , \qquad (56) \\
f^{\text{Ai}}_{\text{c,II}}(k,n) &:= \int_0^{\infty} \cos(kz)\, \text{Ai}\left(\frac{z - z_n}{z_0} \right) \mathrm{d}z, \\
f^{\text{Ai}}_{\text{s,II}}(k,n) &:= \int_0^{\infty} \sin(kz)\, \text{Ai}\left(\frac{z - z_n}{z_0} \right) \mathrm{d}z.
\end{aligned}
$$

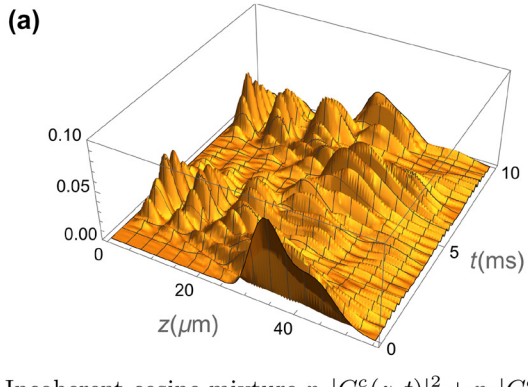

Incoherent cosine mixture $p_1|G^c_1(z,t)|^2 + p_2|G^c_2(z,t)|^2$

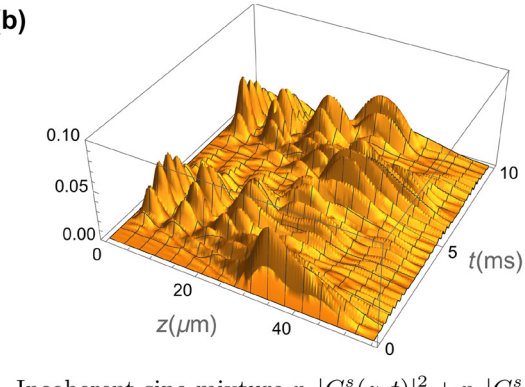

Incoherent sine mixture $p_1|G^s_1(z,t)|^2 + p_2|G^s_2(z,t)|^2$

Figure 19: Incoherent trigonometric mixtures, see Eqs. (49) and (55), in region II with $p_1 = 0.7$ and $p_2 = 0.3$.

This can be expressed as

$$|F_{m,\mathrm{II}}(k,t)|^2 = \left[F^{\mathrm{Re}}_{m,\mathrm{II}}(k,t)\right]^2 + \left[F^{\mathrm{Im}}_{m,\mathrm{II}}(k,t)\right]^2,$$

$$F^{\mathrm{Re}}_{m,\mathrm{II}}(k,t) := \frac{\bar{C}_m}{\sqrt{2\pi}} \sum_{n=1}^{\infty} D_{n,m} \left[\cos\left(\frac{E_n}{\hbar}t\right) f^{\mathrm{Ai}}_{\mathrm{c,II}}(k,n) - \sin\left(\frac{E_n}{\hbar}t\right) f^{\mathrm{Ai}}_{\mathrm{s,II}}(k,n)\right],$$

$$F^{\mathrm{Im}}_{m,\mathrm{II}}(k,t) := -\frac{\bar{C}_m}{\sqrt{2\pi}} \sum_{n=1}^{\infty} D_{n,m} \left[\cos\left(\frac{E_n}{\hbar}t\right) f^{\mathrm{Ai}}_{\mathrm{s,II}}(k,n) + \sin\left(\frac{E_n}{\hbar}t\right) f^{\mathrm{Ai}}_{\mathrm{c,II}}(k,n)\right]. \quad (57)$$

In Figure 20(a) and (b) we present two examples of $|F_{m,\mathrm{II}}(k,t)|^2$ for $m = 1$ and $m = 2$. Figure 20(a) shows the time dependence of the ground state momentum distribution in region II. At $t = 0$ the function $|F_{1,\mathrm{II}}(k,0)|^2$ is the Fourier transform of the approximated wave function of Figure 14(b) squared and has a maximum exactly at $k = 0$. During the evolution of time t the maxima are displaced to larger values of k. This causes an inclined periodic $(t-k)$-pattern of the momentum distribution. For the first excited state ($m = 2$) the pattern is shifted once more, as can be seen in Figure 20(b). At $t = 0$ we can observe a double peak in accordance with the first excited state at the boundary between regions I and II. As expected, there is a distinct minimum at $k = 0$.

4.4 Wigner function

The Wigner function $W_{m,\mathrm{II}}(z,k,t)$ in region II is given in terms of the corresponding wave function $\psi_{m,\mathrm{II}}(z,t)$ from Eq. (44):

$$W_{m,\mathrm{II}}(z,k,t) = \frac{1}{2\pi}\int_{-\infty}^{\infty} \mathrm{e}^{\mathrm{i}z'k} \psi^*_{m,\mathrm{II}}\left(z+\frac{z'}{2},t\right)\psi_{m,\mathrm{II}} \times \left(z-\frac{z'}{2},t\right)\mathrm{d}z', \quad z \geq 0. \quad (58)$$

Proceeding similarly to how we did in Eq. (40), we find the limits of integration to fulfill $-2z \leq z' \leq 2z$. Moreover, we can separate the wave function into two parts using Eq. (49):

$$\psi_{m,\mathrm{II}}(z,t) = G^{\mathrm{c}}_m(z,t) + \mathrm{i}\, G^{\mathrm{s}}_m(z,t). \quad (59)$$

After a simple calculation we obtain the following result for the Wigner function in region II:

$$W_{m,\mathrm{II}}(z,k,t) = \frac{1}{\pi}\int_0^{2z} \mathrm{d}z' \left\{\cos(kz') \times \left[G^{\mathrm{c}}_m\left(z+\frac{z'}{2},t\right) G^{\mathrm{c}}_m\left(z-\frac{z'}{2},t\right) + G^{\mathrm{s}}_m\left(z+\frac{z'}{2},t\right) G^{\mathrm{s}}_m\left(z-\frac{z'}{2},t\right)\right]\right.$$

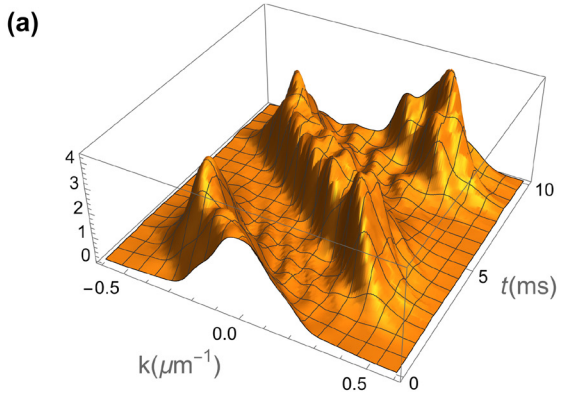

Momentum distribution $|F_{1,\mathrm{II}}(k,t)|^2$; Positive and negative $k-$values are included. We can nicely observe the linear increase of momentum with time and the abrupt sign changes of momentum at the bounces.

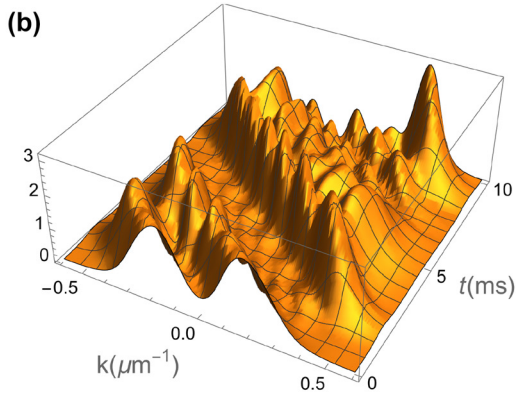

Momentum distribution $|F_{2,\mathrm{II}}(k,t)|^2$

Figure 20: Momentum distributions, see Eq. (57), in region II for the ground state and the first excited state.

$$+\sin(kz')\left[G_m^{\mathrm{s}}\left(z+\frac{z'}{2},t\right)G_m^{\mathrm{c}}\left(z-\frac{z'}{2},t\right)-G_m^{\mathrm{c}}\left(z+\frac{z'}{2},t\right)G_m^{\mathrm{s}}\left(z-\frac{z'}{2},t\right)\right]\Bigg\}. \quad (60)$$

Figure 21(a) and (b) show two examples for $m=1$ at time $t=0$ and $t=3$ ms, respectively. At first, we will discuss the case $t=0$. In this case, the Wigner function reads

$$W_{1,\mathrm{II}}(z,k,0)=\frac{1}{\pi}\int_0^{2z}\mathrm{d}z'\cos(kz')\,G_1^{\mathrm{c}}\left(z+\frac{z'}{2},0\right)G_1^{\mathrm{c}}\times\left(z-\frac{z'}{2},0\right),$$

$$G_1^{\mathrm{c}}(z,0)=\frac{\bar{C}_1}{\sqrt{2\pi}}\sum_{n=1}^{\infty}D_{n,1}\mathrm{Ai}\left(\frac{z-z_n}{z_0}\right). \quad (61)$$

$W_{1,\mathrm{II}}(z,k,0)$ is depicted in Figure 21(a). It is non-vanishing between $z=27$ μm and $z=55$ μm and should be positive almost everywhere. This Wigner function should be approximately the same as in Figure 12(a), where only positive $k-$values have been taken into account and the $z-$values are shifted ($0\le z\le 28$ μm) because no step has been considered there.

At $t=3$ ms the Wigner function takes the shape shown in Figure 21(b). It is clearly more complicated than the shape of the ground state in Figure 21(a), and has multiple local extrema. For the UCNs with a horizontal velocity of $v_0=6m/s$ the time $t=3$ ms chosen for the representation of the Wigner function corresponds to the distance $x=18$ cm from the beginning of region *II*. One can recognize that the Wigner function is strongly compressed at the mirror $z=0$ and starts being reflected whereupon distinct waves appear for $z>0$. Likewise, the reflection of the spatial distributions in Figure 15(a) and in Figure 20(a) for the momentum distribution can be observed in case of $t\approx 3$ ms. By the way, this reflection time of $t\approx 3ms$ can be derived classically from $z=-\frac{g}{2v_0^2}x^2+H$ setting $z=0$ and $x=v_0t$. If we take an average height of free fall of $H=(h+9.1\ \mu\mathrm{m})=36.1$ μm (see Figure 15(a) for $t=0$) the result is $t=\sqrt{2H/g}=2.713$ ms. The corresponding $k-$ value at $z=0$ is $k=-mgt/\hbar=-0.423\ \mu\mathrm{m}^{-1}$. We use $t\approx 3$ ms as a rough value. In Figure 15(a) a high-peaked reflection-wave appears at $z=0$ and in Figure 20(a) the momentum performs a jump from $k\approx -0.4\ \mu\mathrm{m}^{-1}$ to $k\approx 0.4\ \mu\mathrm{m}^{-1}$ because of the reflection at the mirror. Likewise the linear time-evolution of the momentum is seen clearly.

It would be interesting to compare to a classical picture. In case of absence of a mirror the Wigner function Figure 21(a) falls down to $z=0$ and then gains negative values $z<0$ always keeping the same structure. In case of a mirror the same Wigner function would be reflected at $z=0$ and attains regions of $z>0$ bouncing like a ball. Most suitable is again Figure 15(a) where the quantum mechanical spacial distribution is drawn. The classical parabolic time-course $z=-\frac{g}{2}t^2+H$ is apparent and the reflection at $t\approx 3$ ms and then the recovery to the initial position and so on.

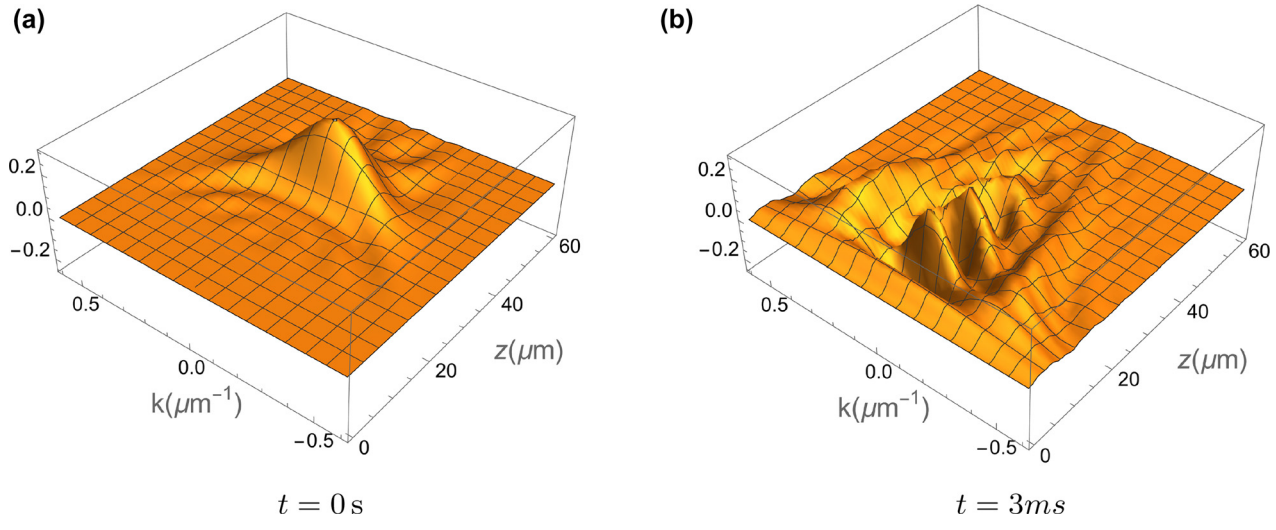

Figure 21: Evolution of the Wigner function $W_{1,\mathrm{II}}(z,k,0)$ of the ground state in region II, see Eq. (60).

5 Including a Yukawa-like term in region II

It is interesting to include a small perturbation to the potential in the Schrödinger equation in order to simulate a small variation of the gravitational field near the mirror. The basic idea behind this proposal is to modify gravity at small distances and determine the limits on non-Newtonian gravitation below 10 μm.

5.1 First order perturbation calculation and a new wave function

When a neutron with mass m_N approaches the mirror, the mass of this extended source might modify the gravitational acceleration of Earth g due to a potentially present non-Newtonian force with range δ, see Ref. [21]. This modification would lead to an additional, Yukawa-type interaction

$$W(z) = W_0\, \mathrm{e}^{-\frac{\zeta}{(\delta/z_0)}}. \tag{62}$$

The parameter W_0 is a positive or negative constant with the dimension of an energy and δ is called Yukawa-distance over which the corresponding force acts. δ is measured in units of z_0. The stationary Schrödinger Eq. (4) reads now

$$\left[-\frac{\hbar^2}{2m_N}\frac{\mathrm{d}^2}{\mathrm{d}z^2} + m_N g z + W(z)\right]\Psi_n^{\mathrm{Yu}}(z) = \epsilon_n \Psi_n^{\mathrm{Yu}}(z). \tag{63}$$

$\Psi_n^{\mathrm{Yu}}(z)$ and ϵ_n are the corresponding wave functions and energy eigenvalues. The quantity $W(z)$ has to be a small correction to $m_N g z$. In the basis of normalized Airy-functions given in Eq. (9) we obtain at first order:

$$\epsilon_n = E_n + E_n^{(1)}, \tag{64}$$

$$\Psi_n^{\mathrm{Yu}}(z) = \psi_n(z) + \psi_n^{(1)}(z), \tag{65}$$

where

$$E_n^{(1)} = \langle\psi_n|W|\psi_n\rangle = \int_0^\infty |\psi_n(z)|^2\, W(z)\,\mathrm{d}z, \tag{66}$$

$$\begin{aligned}\psi_n^{(1)}(z) &= \sum_{n'\neq n}\frac{\langle\psi_{n'}|W|\psi_n\rangle}{E_n - E_{n'}}\psi_{n'}(z)\\ &= \sum_{n'\neq n}\frac{J_{n',n}}{E_n - E_{n'}}\psi_{n'}(z)\end{aligned} \tag{67}$$

with

$$J_{n',n} := \int_0^\infty \left[\psi_{n'}(z')\right]^*\, W(z')\,\psi_n(z')\,\mathrm{d}z'. \tag{68}$$

Note that $\langle\psi_n|\psi_n\rangle = 1$, $\langle\psi_n|\psi_n^{(1)}\rangle = 0$, $\left\langle\psi_n|\Psi_n^{\mathrm{Yu}}\right\rangle = 1$ and $\left\langle\Psi_n^{\mathrm{Yu}}|\Psi_n^{\mathrm{Yu}}\right\rangle \approx 1$.

In Figure 22(a) the total potential $V(z) = m_N g z + W(z)$ is drawn for $W_0 = 0$ and for an additional attractive potential with the strength $W_0 = -1$ peV. Since the total force is therefore given by $\vec{K}(z) = -\vec{\nabla}V(z) = \left[-mg + \frac{W_0}{\delta}\,\mathrm{e}^{-z/\delta}\right]\mathbf{e}_z$, we can see that the Yukawa-potential leads to an additional force. Figure 22(b) shows ϵ_n as a function of $-W_0$. The eigenvalues ϵ_n decrease with increasing W_0.

Next, we write the eigenfunctions (65) in the form

$$\begin{aligned}\Psi_n^{\mathrm{Yu}}(z) &= \psi_n(z) + \sum_{n'\neq n}\frac{J_{n',n}}{E_n - E_{n'}}\psi_{n'}(z)\\ &=: \sum_{n'}\psi_{n'}(z)\; T_{n',n}.\end{aligned} \tag{69}$$

$T_{n',n}$ is a unit matrix but with small off-diagonal terms proportional to W_0 that represent the small numbers $J_{n',n}$.

For simplicity, we neglect the modifications of the neutron wave function at $t = 0$ by the Yukawa interaction in region I and consequently assume that the wave function in region II resembles the one in Eq. (44), but with a yet unknown form of $\psi_{n'}(z)$:

$$\begin{aligned}\psi_{m,\mathrm{II}}^{\mathrm{Yu}}(z) &= \bar{C}_m \sum_{n'}\psi_{n'}(z)\,\bar{D}_{n',m} \quad \text{with}\\ \bar{D}_{n',m} &:= D_{n',m}\,\sqrt{z_0}\,\mathrm{Ai}'\left(-\frac{z_{n'}}{z_0}\right).\end{aligned} \tag{70}$$

From Eq. (69) we can extract $\psi_{n'}(z)$ by means of the following approach: multiplying from the right by $T^{-1}_{n,n''}$ and summing over n we obtain

$$\begin{aligned}\sum_n \Psi_n^{\mathrm{Yu}}(z)T^{-1}_{n,n''} &= \sum_{n'}\psi_{n'}(z)\sum_n T_{n',n}T^{-1}_{n,n''}\\ &= \sum_{n'}\psi_{n'}(z)\,\delta_{n',n''} = \psi_{n''}(z).\end{aligned} \tag{71}$$

Inserting this relation into Eq. (70), we get the modification of Eq. (44) for Yukawa forces

$$\psi_{m,\mathrm{II}}^{\mathrm{Yu}}(z) = \bar{C}_m \sum_{n,n'}\Psi_n^{\mathrm{Yu}}(z)T^{-1}_{n,n'}\bar{D}_{n',m}. \tag{72}$$

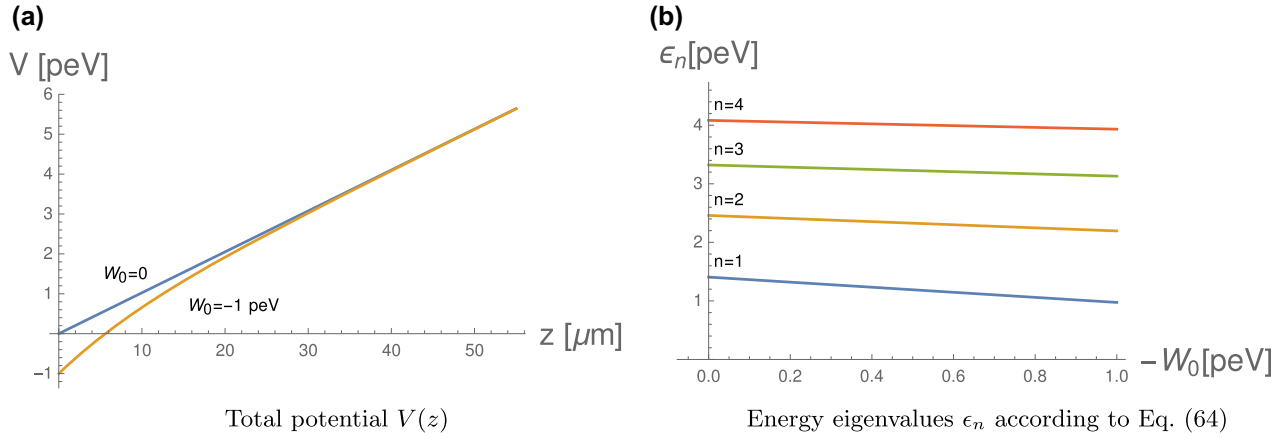

Total potential $V(z)$ Energy eigenvalues ϵ_n according to Eq. (64)

Figure 22: Total potential $V(z) = m_N g z + W(z)$ and energy eigenvalues $\epsilon_n(W_0)$ for a Yukawa-distance $\delta = 10$ μm.

Taking into account the time dependence of the eigenfunctions from Eq. (69) in region II

$$\Psi_n^{\mathrm{Yu}}(z,t) = \Psi_n^{\mathrm{Yu}}(z) \exp\left[-\frac{\mathrm{i}}{\hbar}\epsilon_n t\right], \tag{73}$$

we get the time evolution of the perturbed wave function from Eq. (72) in region II:

$$\psi_{m,\mathrm{II}}^{\mathrm{Yu}}(z,t) = \bar{C}_m \sum_{n',n''} \psi_{n'}(z) \times \left\{ \sum_n T_{n',n} \exp\left[-\frac{\mathrm{i}}{\hbar}\epsilon_n t\right] \; T^{-1}_{n,n''} \right\} \bar{D}_{n'',m}. \tag{74}$$

For vanishing Yukawa forces, $T_{n\prime,n} = \delta_{n\prime,n}$ and $\epsilon_n = E_n$, this equation reduces to Eq. (44).

5.2 Space distribution with Yukawa correction in region II

We separate the real and imaginary parts of the wave function in Eq. (74):

$$\begin{aligned}
\mathrm{Re}_\psi &= \bar{C}_m \sum_{n',n''} \psi_{n'}(z) \times \left\{ \sum_n T_{n',n} \cos\left(\frac{\epsilon_n}{\hbar} t\right) \; T^{-1}_{n,n''} \right\} \bar{D}_{n'',m}, \\
\mathrm{Im}_\psi &= \bar{C}_m \sum_{n',n''} \psi_{n'}(z) \times \left\{ \sum_n T_{n',n} \sin\left(\frac{\epsilon_n}{\hbar} t\right) \; T^{-1}_{n,n''} \right\} \bar{D}_{n'',m},
\end{aligned} \tag{75}$$

such that

$$|\psi_{m,\mathrm{II}}^{\mathrm{Yu}}(z,t)|^2 = \mathrm{Re}_\psi^2 + \mathrm{Im}_\psi^2. \tag{76}$$

An interesting way of comparing space distributions with and without Yukawa interaction is the following quantity:

$$\Delta_{\mathrm{Yu}}(z,t) := |\psi_{m,\mathrm{II}}^{\mathrm{Yu}}(z,t)|^2 - |\psi_{m,\mathrm{II}}(z,t)|^2. \tag{77}$$

Here $|\psi_{m,\mathrm{II}}(z,t)|^2$ is given in Eq. (50) or, equivalently, by Eq. (76) when setting $W_0 = 0$.

In Figure 23(a) we assume $W_0 = -1$ peV and draw the corresponding $\Delta_{\mathrm{Yu}}(z,t)$. For comparison, we also depicted $|\psi_{m,\mathrm{I}}^{\mathrm{Yu}}(z,t)|^2$ in Figure 23(b). For $t = 0$ this function is exactly the same as in Figure 15(a). However, for $t > 0$, small differences to the function shown in Figure 15(a) can be noticed.

5.3 Momentum distribution of Yukawa correction in region II

Next, we want to look at the momentum distribution and therefore consider the Fourier transform of the wave function in Eq. (74), which is given by (compare with Eq. (56))

$$\begin{aligned}
F_{m,\mathrm{II}}^{\mathrm{Yu}}(k,t) = \frac{\bar{C}_m}{\sqrt{2\pi}\sqrt{z_0}} \sum_{n',n''} \frac{1}{\mathrm{Ai}'\left(-\frac{z_{n'}}{z_0}\right)} \\
\times \left[f_{\mathrm{c,II}}^{\mathrm{Ai}}(k,n') - \mathrm{i} f_{\mathrm{s,II}}^{\mathrm{Ai}}(k,n') \right] \\
\times \left\{ \sum_{\mathrm{N}} T_{n',n} \left[\cos\left(\frac{\epsilon_n}{\hbar} t\right) \right.\right. \\
\left.\left. - \mathrm{i} \sin\left(\frac{\epsilon_n}{\hbar} t\right) \right] \right\} T^{-1}_{n,n''} \Bigg\} \bar{D}_{n'',m}.
\end{aligned} \tag{78}$$

The real and the imaginary part of this expression are

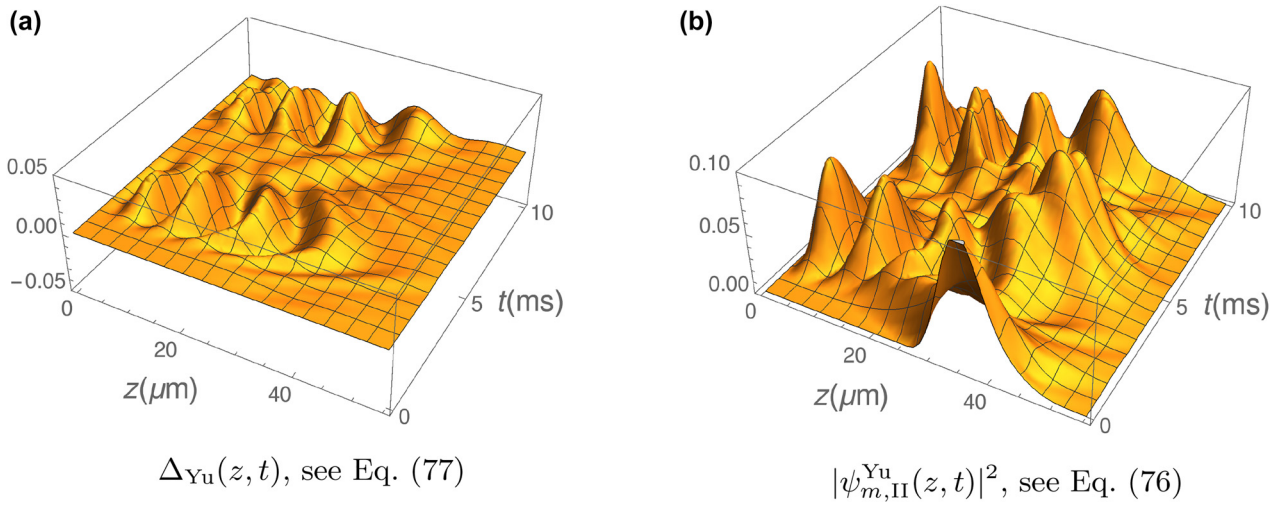

$\Delta_{\mathrm{Yu}}(z,t)$, see Eq. (77)

$|\psi^{\mathrm{Yu}}_{m,\mathrm{II}}(z,t)|^2$, see Eq. (76)

Figure 23: Difference in spatial distributions with and without Yukawa interaction, and spatial distribution with Yukawa interaction; $m = 1$, $\delta = 10$ μm and $W_0 = -1$ peV.

$$\mathrm{Re}_F = \frac{\bar{C}_m}{\sqrt{2\pi}\sqrt{z_0}} \sum_{n',n''} \frac{1}{\mathrm{Ai}'\left(-\frac{z_{n'}}{z_0}\right)} \times \left\{ f^{\mathrm{Ai}}_{\mathrm{c,II}}(k,n') \sum_n T_{n',n} \cos\left(\frac{\epsilon_n}{\hbar} t\right) T^{-1}_{n,n''} - f^{\mathrm{Ai}}_{\mathrm{s,II}}(k,n') \sum_n T_{n',n} \sin\left(\frac{\epsilon_n}{\hbar} t\right) T^{-1}_{n,n''} \right\} \bar{D}_{n'',m},$$

$$\mathrm{Im}_F = -\frac{\bar{C}_m}{\sqrt{2\pi}\sqrt{z_0}} \sum_{n',n''} \frac{1}{\mathrm{Ai}'\left(-\frac{z_{n'}}{z_0}\right)} \times \left\{ f^{\mathrm{Ai}}_{\mathrm{s,II}}(k,n') \sum_n T_{n',n} \cos\left(\frac{\epsilon_n}{\hbar} t\right) T^{-1}_{n,n''} + f^{\mathrm{Ai}}_{\mathrm{c,II}}(k,n') \sum_n T_{n',n} \sin\left(\frac{\epsilon_n}{\hbar} t\right) T^{-1}_{n,n''} \right\} \bar{D}_{n'',m}, \quad (79)$$

such that

$$|F^{\mathrm{Yu}}_{m,\mathrm{II}}(k,t)|^2 = \mathrm{Re}_F^2 + \mathrm{Im}_F^2. \quad (80)$$

Setting $W_0 = 0$ in Eq. (79) recovers Eq. (57), which gives the expression for $|F_{m,\mathrm{II}}(k,t)|^2$.

An interesting way of comparing the momentum distributions with and without Yukawa interaction is the following quantity:

$$\Delta_{\mathrm{Yu}}(k,t) = |F^{\mathrm{Yu}}_{m,\mathrm{II}}(k,t)|^2 - |F_{m,\mathrm{II}}(k,t)|^2. \quad (81)$$

In Figure 24(a) this difference of the momentum distributions with and without Yukawa interaction is depicted. At the jump discontinuities $t \approx 3$ ms and $t \approx 9$ ms distinct differences are visible. At these times the wave function is reflected at the mirror where the Yukawa potential is the strongest. This can also be observed in Figure 24(b), in which $|F^{\mathrm{Yu}}_{m,\mathrm{II}}(k,t)|^2$ is shown. At these points in time $|F^{\mathrm{Yu}}_{m,\mathrm{II}}(k,t)|^2$ exhibits distinct maxima compared to the momentum distribution without Yukawa interaction depicted in Figure 20(a).

5.4 Discussion and proposed applications of Yukawa correction in region II

It would be interesting to apply the proposed procedure of Yukawa correction $W(z)$ of the Newtonian gravitational energy $m_N gz$ (see Eq. (62), Eq. (63) and Figure 22(a)) and compare the calculated results to real experimental data. Since the experiment is still running a direct precise comparison between theory and experiment will be possible in the near future.

At the present time the experimental focus is directed to the measurement of the space distribution immediately at the double mirror system (at time $t = 0$) and at a certain distance in region II (say 5 or 6 cm, which is equivalent to a few microseconds). The calculated space distribution $|\psi_{1,\mathrm{II}}(z,t)|^2$ (without Yukawa-correction) for the ground state is drawn in Figure 15(a). At $t = 0$ one can directly observe the space distribution of the ground state at the very beginning of the region II. In general the computed space distribution will not have exactly the experimental shape (see Ref. [26], Ref. [28], Ref. [23], Ref. [25]). For example, a fit to the data at $t = 0$ (see Ref. [23]) is approximately comparable to an incoherent mixture of the ground-state population of 70% and a first excited-state population of 30%. This case is presented in Figure 18(a). However, other mixtures are possible. At a distance of

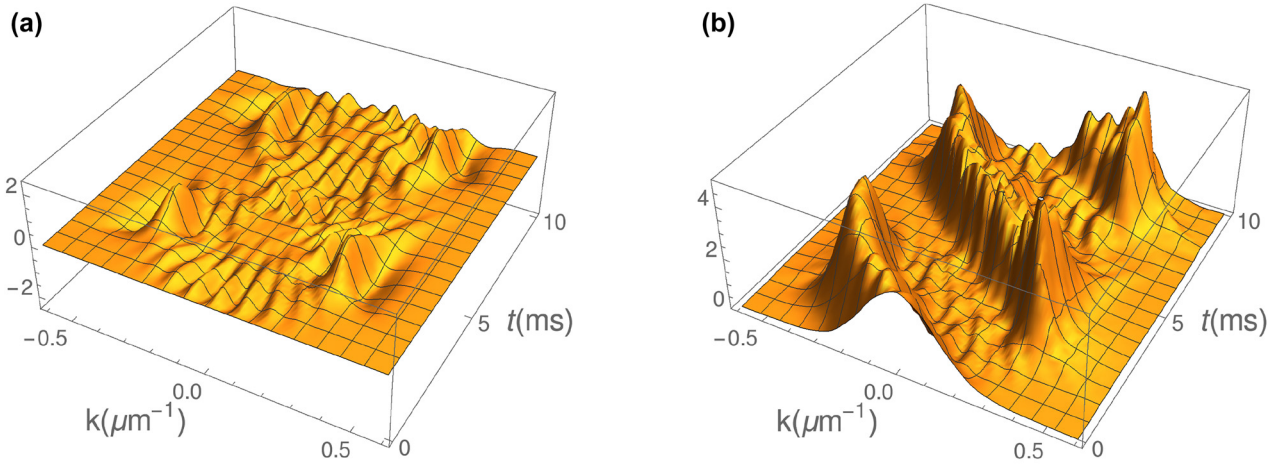

$\Delta_{\mathrm{Yu}}(k,t)$, see Eq. (81) $|F^{\mathrm{Yu}}_{m,\mathrm{II}}(k,t)|^2$, see Eq. (80)

Figure 24: Difference in momentum distributions with and without Yukawa interaction, and momentum distribution with Yukawa interaction; $m = 1$, $\delta = 10$ μm and $W_0 = -1$ peV.

5.1 cm in region II measured values have been reported (Ref. [25]).

We now propose the following procedure:

(1) We did not consider Yukawa-corrections in region I. Therefore we suggest to execute a fit of measured data at the time $t = 0$ (i.e. $x = 0$ cm) at its best by using e.g. an incoherent mixture of ground state and first excited state of the space distribution in region II seen in Figure 18(a).

(2) If the velocity of neutron wave amounts to 6 m/s then after $t = 10$ ms the wave has covered a distance of $x = 6$ cm where a detector could compare the measurement with the theoretical prediction as shown in the time-dependent space distribution of Figure 18(a).

(3) If significant differences between experimental and theoretical results are observed, the Yukawa-like term has to be considered in region II as described in Sections 5.1 and 5.2 of this chapter 5. We have 2 parameters which can be adjusted to the experimental results. These parameters are related to the Yukawa correction $W(z)$ seen in Eq. (62): The strength parameter W_0 is a positive or negative constant with the dimension of an energy and the Yukawa-distance δ determines the distance over which the corresponding force acts. In Figure 22(a) an example is given for $W_0 = -1$ peV and $\delta = 10$ μm. Parameter values W_0 and δ should be found which best approximate the experimental results. These optimal parameters would indicate the evidence of a non-Newtonian contribution to the common Newton potential near the surface of the mirror.

Generally speaking, the dynamics of exact quantum mechanical treatment of the qBounce problem combines quantum theory with aspects of Newtonian mechanics at short distances. Newtonian gravity and non-Newtonian hypothetical fifths forces evolve with different phase information because of modified energy eigenvalues due to Yukawa correction (see Figure 22(b)). In this respect the investigation presented in this paper could contribute to a direct search for dark matter.

6 Conclusions

In this theoretical treatise the wave function of the *q*Bounce experiment has been investigated in detail. The gravitational field of the Earth constitutes the potential used in the Schrödinger equation. This yields solutions for the wave function which correspond to the Airy function. Since the wave function has to vanish at the mirror surface, a ground state and excited states evolve. These states have been analyzed with respect to spatial and momentum distributions. For this purpose, the Wigner function has also been used. It was shown that the distribution spectra of the ground and excited states exhibit the anticipated properties, which are reproduced in the marginal distribution functions. Furthermore, the time dependence of a mixture of the ground state and the first excited state has been considered. The *q*Bounce-problem in which the neutron wave is enclosed between 2 mirrors has

been analyzed as well. Finally, the case where the wave function exits the double mirror system and freely falls on a subsequent mirror has been considered. The purpose of these calculations was to motivate measurements both in real space and in momentum space for comparison between experimental findings and theoretical results. Finally and in addition, we made an attempt at a first order perturbation calculation in order to describe a very small change in the potential near the mirror due to a Yukawa-like coupling. Already from this very simplified calculation we predicted differences in the spatial and momentum distributions between cases with and without a Yukawa-like interaction. However, in order to make a statement about a realistic experimental situation, the probability distribution of neutrons at the transition from region I to region II should be known in detail when also taking into account the Yukawa-like interaction in region I. Though, this is beyond the scope of this article since a much more intricate computation would be required.

Author contribution: All the authors have accepted responsibility for the entire content of this submitted manuscript and approved submission.
Research funding: This work was supported by the Austrian Science Fund (FWF): P 34240-N.
Conflict of interest statement: The authors declare no conflicts of interest regarding this article.

References

[1] J. Gea-Banacloche, "A quantum bouncing ball," *Am. J. Phys.*, vol. 67, no. 9, pp. 776–782, 1999.
[2] R. L. Gibbs, "The quantum bouncer," *Am. J. Phys.*, vol. 43, no. 1, pp. 25–28, 1975.
[3] P. W. Langhoff, "Schrödinger particle in a gravitational well," *Am. J. Phys.*, vol. 39, no. 8, pp. 954–957, 1971.
[4] D. A. Goodings and T. Szeredi, "The quantum bouncer by the path integral method," *Am. J. Phys.*, vol. 59, no. 10, pp. 924–930, 1991.
[5] S. Whineray, "An energy representation approach to the quantum bouncer," *Am. J. Phys.*, vol. 60, no. 10, pp. 948–950, 1992.
[6] R. D. Desko and D. J. Bord, "The quantum bouncer revisited," *Am. J. Phys.*, vol. 51, no. 1, pp. 82–84, 1983.
[7] S. T. Dembiński and L. Wolniewicz, "Remarks on solving the one-dimensional time-dependent Schrödinger equation on the interval : the case of a quantum bouncer," *J. Phys. A: Math. Gen.*, vol. 29, no. 2, pp. 349–355, 1996.
[8] S. T. Dembiński, A. J. Makowski, and P. Pepłowski, "Quantum bouncer with chaos," *Phys. Rev. Lett.*, vol. 70, 1093–1096, 1993.
[9] O. Vallee and M. Soares, *Airy Functions and Applications to Physics*, 2nd ed. London, UK, Imperial College Press, 2010.
[10] E. Giese, W. Zeller, S. Kleinert, et al., "The interface of gravity and quantum mechanics illuminated by Wigner phase space," in *Proceeding of the International School of Physics "Enrico Fermi", Course 188 "At. Interferometry"*, G. M. Tino, and M. A. Kasevich, Eds., Amsterdam; SIF, Bologna, IOS Press, 2014, pp. 171–236.
[11] F. Saif, G. Alber, V. Savichev, and W. P. Schleich, "Quantum revivals in a periodically driven gravitational cavity," *J. Opt. B: Quantum Semiclass. Opt.*, vol. 2, no. 5, pp. 668–671, 2000.
[12] E. Kajari, N. L. Harshman, E. M. Rasel, S. Stenholm, G. Süßmann, and W. P. Schleich, "Inertial and gravitational mass in quantum mechanics," *Appl. Phys. B*, vol. 100, no. 1, pp. 43–60, 2010.
[13] V. V. Nesvizhevsky, H. G. Börner, A. K. Petukhov, et al., "Quantum states of neutrons in the Earth's gravitational field," *Nature*, vol. 415, no. 6869, pp. 297–299, 2002.
[14] V. V. Nesvizhevsky, H. G. Börner, A. M. Gagarski, et al., "Measurement of quantum states of neutrons in the Earth's gravitational field," *Phys. Rev. D*, vol. 67, no. 10, p. 102002, 2003.
[15] V. V. Nesvizhevsky, A. K. Petukhov, H. G. Börner, et al., "Study of the neutron quantum states in the gravity field," *Eur. Phys. J. C*, vol. 40, no. 4, pp. 479–491, 2005.
[16] A. Y. Voronin, H. Abele, S. Baessler, et al., "Quantum motion of a neutron in a waveguide in the gravitational field," *Phys. Rev. D*, vol. 73, no. 4, p. 044029, 2006.
[17] A. Westphal, H. Abele, S. Baessler, V.V. Nesvizhevsky, K.V. Protasov, and A.Y. Voronin, "A quantum mechanical description of the experiment on the observation of gravitationally bound states," *Eur. Phys. J. C*, vol. 51, no. 2, pp. 367–375, 2007.
[18] H. Abele, S. Baessler, and A. Westphal, "Quantum states of neutrons in the gravitational field and limits for non-Newtonian interaction in the range between 1 μm and 10 μm," in *Quantum gravity: From theory to experimental search, Lecture Notes in Physics*, D. J. W. Giulini, C. Kiefer, and C. Laemmerzahl, Eds., Berlin, Heidelberg, Springer, 2003, pp. 355–366.
[19] V. V. Nesvizhevsky and K. V. Protasov, "Constraints on non-Newtonian gravity from the experiment on neutron quantum states in the earth's gravitational field," *Class. Quantum Grav.*, vol. 21, no. 19, pp. 4557–4566, 2004.
[20] S. Baeßler, V. V. Nesvizhevsky, K. V. Protasov, and A. Y. Voronin, "Constraint on the coupling of axionlike particles to matter via an ultracold neutron gravitational experiment," *Phys. Rev. D*, vol. 75, p. 075006, 2007.
[21] H. Abele, T. Jenke, H. Leeb, and J. Schmiedmayer, "Ramsey's method of separated oscillating fields and its application to gravitationally induced quantum phase shifts," *Phys. Rev. D*, vol. 81, no. 6, p. 065019, 2010.
[22] T. Jenke, P. Geltenbort, H. Lemmel, and H. Abele, "Realization of a gravity-resonance-spectroscopy technique," *Nat. Phys. Lett.*, vol. 7, pp. 468–472, 2011.
[23] T. Jenke, G. Cronenberg, J. Burgdörfer, et al., "Gravity resonance spectroscopy constrains dark energy and dark matter scenarios," *Phys. Rev. Lett.*, vol. 112, no. 15, p. 151105, 2014.

[24] G. Cronenberg, P. Brax, H. Filter, et al., "Acoustic Rabi oscillations between gravitational quantum states and impact on symmetron dark energy," *Nat. Phys.*, vol. 14, no. 10, pp. 1022–1026, 2018.
[25] T. Jenke, G. Cronenberg, M. Thalhammer, B. Rechberger, B. Geltenbort, and H. Abele, "Gravity experiments with ultracold neutrons and the qbounce experiment," arXiv:1510.03078v1 [physics.ins-det], 2015.
[26] H. Abele, T. Jenke, D. Stadler, and P. Geltenbort, "QuBounce: the dynamics of ultra-cold neutrons falling in the gravity potential of the earth," *Nucl. Phys.*, vol. 827, no. 1, pp. 593c–595c, 2009.
[27] J. Tobias, D. Stadler, H. Abele, and P. Geltenbort, "Q-BOUNCE - experiments with quantum bouncing ultracold neutrons," *Nucl. Instrum. Methods Phys. Res. Sect. A Accel. Spectrom. Detect. Assoc. Equip.*, vol. 611, no. 2, pp. 318–321, 2009.
[28] H. Abele and H. Leeb, "Gravitation and quantum interference experiments with neutrons," *New J. Phys.*, vol. 14, no. 5, p. 055010, 2012.
[29] J. Tobias, C. Gunther, H. Filter, et al., "Ultracold neutron detectors based on 10B converters used in the qBounce experiments," *Nucl. Instrum. Methods Phys. Res. Sect. A Accel. Spectrom. Detect. Assoc. Equip.*, vol. 732, pp 1–8, 2013.
[30] M. Pitschmann, "Remarks on qbounce," Private Communication, 2018.
[31] W. P. Schleich, *Quantum Optics in Phase Space*, 1st ed. Berlin, Wiley-VCH, 2001.
[32] M. Pitschmann and H. Abele, "Schrödinger equation for a non-relativistic particle in a gravitational field confined by two vibrating mirrors," arXiv:1912.12236v1 [quant-ph], 2019.